Energy Conversion and Management 350 (2026) 120936

Contents lists available at ScienceDirect

Energy Conversion and Management

journal homepage: www.elsevier.com/locate/enconman

Research Paper

Advanced air supply system topologies for fuel cells in aircraft applications

Matthias Schröder [a,*], Christoph Gentner [a], Syed-Asif Ansar [b]

[a] German Aerospace Center (DLR), Institute of Engineering Thermodynamics, Hein-Saß-Weg 22, 21129 Hamburg, Germany
[b] German Aerospace Center (DLR), Institute of Engineering Thermodynamics, Pfaffenwaldring 38-40, 70569 Stuttgart, Germany

ARTICLE INFO

Keywords:
Fuel cell system
Aviation
Compressor
Turbine
Propulsion
Auxiliary power

ABSTRACT

Proton exchange membrane fuel cells hold great promise as a power source for future low-emission aircraft. However, the reduced ambient pressure at high altitudes poses challenges for the reactant air supply to the fuel cells. We introduce several advanced topologies for the fuel cell's air supply and analyze them with a thermodynamic model, which uniquely accounts for interactions with the stack, humidifier, and thermal management system. The results show that the optimal topology depends on the aircraft type. For the propulsion of regional aircraft, an added turbine stage can reduce the mass of the fuel cell system and tank by 4.5 %; whereas for auxiliary power in larger aircraft, two-stage compression enables a 10.9 % efficiency gain during cruise. These findings underscore the importance of tailored air supply solutions for fuel cell systems and provide a pathway towards improving their performance in aircraft applications.

1. Introduction

Commercial aviation is responsible for approximately 4 % of human-induced global warming [1] and is a particularly hard-to-abate sector [2]. As passenger numbers continue to rise, the emissions of aviation are projected to increase further [3]. In response, there is an urgent need to decarbonize future aircraft, and one promising approach to reduce the emissions of future aircraft designs is to replace conventional jet fuel with hydrogen produced from renewable sources [4]. Hydrogen can be utilized in three distinct ways as an aviation fuel. Firstly, it can serve as feedstock for the production of synthetic kerosene (power-to-liquid). This approach requires only minor modifications to the engines, but faces the challenge of a high fuel production cost [5]. Secondly, hydrogen can be directly combusted in modified gas turbine engines. However, the volumetric energy density of hydrogen is much lower than that of conventional jet fuel, even if the hydrogen is stored in liquid form (gaseous H2, 700 bar: 4.8 MJ/L, liquid H2: 8.5 MJ/L, jet fuel: 34.9 MJ/L) [6]. Thus, extensive modifications of the aircraft would be required to store a sufficient amount of hydrogen. Moreover, the combustion of hydrogen raises the challenge of mitigating NOx emissions, despite potentially lower costs of liquified hydrogen compared to synthetic kerosene [7]. The third option is to use fuel cells to convert the hydrogen's chemical energy into electric energy. Fuel cells can either be used to drive propellers with electric motors [8,9], or to provide electric auxiliary power onboard the aircraft [10,11]. In this context, proton exchange membrane (PEM) fuel cells have emerged as a particularly promising technology for aviation because of their high efficiency and inherently low emissions. Fuel cells can achieve system-level efficiencies of around 50 %, which is higher than the efficiency of small turboprop engines and electric generators that are coupled to large turbofan engines [11,12].

Notwithstanding their advantages, PEM fuel cell systems face critical challenges for their application in aviation. The low ambient pressure at high flight altitudes imposes stringent requirements for the air supply of the fuel cell stacks. The ambient air needs to be highly compressed to achieve feasible stack operating pressures of > 1 bar, which reduces the overall system efficiency and increases the mass of the air supply system [13]. This is a significant drawback as the specific power of fuel cell systems needs to improve substantially in order to become competitive to conventional engines [4]. The EU's Strategic Research and Innovation Agenda targets a system-level specific power of 2.0 kW/kg by the year 2030, the state-of-the-art is 0.5–0.75 kW/kg [14,15]. A high fuel cell system efficiency is important to minimize the additional volume that is required for the hydrogen tanks. Furthermore, state-of-the-art low temperature PEM fuel cell systems require liquid cooling to achieve power outputs of several hundred kW. The liquid cooling system penalizes the aircraft performance because of its added mass and aerodynamic drag [16]. Air-cooled low temperature PEM fuel cells could enable a simplified thermal management, but are currently only available for lower power requirements [17,18]. In addition, air-cooled high temperature PEM fuel cells could become a promising alternative once a

* Corresponding author.
E-mail address: matthias.schroeder@dlr.de (M. Schröder).

https://doi.org/10.1016/j.enconman.2025.120936
Received 17 July 2025; Received in revised form 23 October 2025; Accepted 10 December 2025
Available online 15 December 2025

Nomenclature

Symbol	Description
c_p	Specific heat capacity ($J\,kg^{-1}K^{-1}$)
F_d	Drag force (N)
h	Specific enthalpy (J/kg)
m	Mass (kg)
$\dot{m}$	Mass flow (kg/s)
N	Number of components (−)
p	Pressure (Pa)
P	Electric power (W)
$\dot{Q}$	Heat flow (W)
R_{sp}	Specific gas constant ($J\,kg^{-1}K^{-1}$)
RH	Relative humidity (−)
T	Temperature (K, °C)
V	Volume (m^3)
X	Molar fraction (−)

Greek symbols

η	Efficiency (−)
Π	Pressure ratio (−)

Subscripts

ar	anode recirculation
amb	ambient
aux	auxiliary
av	available
bp	bypass
ccp	compressor coolant loop
cp	compressor
dr	diffuser
eff	effective
el	electric
gf	ground fans
hm	humidifier
hx	heat exchanger
in	inlet
max	maximum
norm	normalized
nz	nozzle
out	outlet
ph	preheater
pu	coolant pump
red	reduced
ref	reference condition
req	required
sh	shaft
s1	stage 1
s2	stage 2
sat	saturation
sys	system-level
tb	turbine
tot	total

sufficient technology readiness level is reached [19].

Previous studies have assessed various ways to improve the performance of fuel cell systems for aviation. Massaro et al. [8] investigated the feasibility of a fuel cell-based propulsion system for a regional aircraft. Their results show that the fuel cell system's efficiency and mass can be improved by operating the stacks below their nominal maximum load. Sparano et al. [20] studied a regional aircraft that uses PEM fuel cells in combination with batteries. They proposed a combined approach for the component sizing and energy management that improves the mass and volume of the powertrain. Zhang et al. [13] studied the sensitivity of the stack performance to various operating conditions and derived an optimized control strategy for self-humidifying PEM fuel cells under aviation conditions. Sain et al. [21] designed a PEM fuel cell system for regional aircraft propulsion and compared different options for the geometric arrangement of the air- and thermal-management subsystems. Kösters et al. [16] proposed an innovative phase-change-heat-pump cooling strategy for a MW-scale PEM fuel cell system. Their simulation results show that phase-change-heat-pump cooling can reduce the cooling drag compared to conventional liquid cooling. Moslehi et al. [22] optimized the performance of a fuel cell/battery hybrid powertrain by developing an energy management strategy that explicitly considers the constraints of the air supply system. In a previous study [12], we developed an approach for the preliminary design of fuel cell systems for regional aircraft propulsion. The proposed approach identifies the smallest feasible combination of fuel cell system components by optimizing the stack operating conditions for each flight phase.

The above studies used a variety of different topologies to compress the ambient air for the fuel cell stacks. For example, refs. [8,12,13,22] considered a single-stage compressor, Ref. [16] considered a single-stage compressor that is coupled to a turbine, and Ref. [21] considered the option of multiple parallel compressor stages. However, all these studies have in common that they only investigated one of these topologies for their respective case. Campanari et al. [23] showed that a thorough comparison of different air supply system topologies for a given application can substantially improve the system performance. While these previous studies made important contributions towards adapting fuel cell systems for aviation, there is a need for a holistic understanding of the system-level effects of different air supply system topologies across varying flight conditions. This scientific gap limits our technological ability to design lightweight and efficient fuel cell systems for high-altitude operation, which in our view is the most critical bottleneck for hydrogen-powered fuel cell systems in aviation. This work addresses this gap with the following contributions:

1. We introduce and rigorously compare a number of advanced topologies for the air supply of fuel cells in aircraft applications. The investigated topologies are as follows: The air can be compressed in a single-stage compression process or in a two-stage compression process. The two compressor stages can be arranged in series to improve the maximum pressure ratio, or in parallel to enlarge the range of feasible mass flows. Moreover, each compressor type can be combined with a turbine stage to recover energy from the fuel cell exhaust. These design choices result in six possible topologies.
2. The potential of these topologies is analyzed with a detailed thermodynamic model. Crucially, the model includes both direct effects related to the air supply system and indirect effects that arise from the coupling to the stacks, humidifier and thermal management system. This enables an improved understanding of the benefits and drawbacks of the above design choices.
3. The effects of different flight altitudes and power requirements on the choice of the optimal air supply system topology are investigated for two promising case studies for fuel cells in aviation: the propulsion of regional aircraft and the auxiliary power supply in larger narrow-body aircraft.

These contributions provide a pathway towards improving the specific power and efficiency of fuel cell systems in aviation by introducing custom-tailored air supply systems for high-altitude operation. In addition to the two investigated aircraft types, the proposed approach can also be applied for other aircraft sizes because the component models

are scalable to different power requirements.

2. Air supply system topologies

The two aircraft concepts that serve as case studies for this study are briefly introduced below; a more detailed description can be found in refs. [12,24,25]. The regional aircraft concept is designed by Atanasov [24] and is shown in Fig. 1 (a). The aircraft is designed to carry 70 passengers; its size is similar to a conventional ATR-72 aircraft [26]. The aircraft uses ten identical fuel cell systems to generate thrust with electrically-driven propellers. The arrangement of ten propellers along the wingspan was chosen to utilize the aircraft-level efficiency gains that can be achieved with such a distributed propulsion concept [27]. Each of the ten fuel cell systems provides 312 kW at takeoff and 273 kW during the cruise phase at an altitude of up to 8840 m. The detailed electric load profile is discussed in Section 4.1.

The narrow-body aircraft is described in Ref. [25] and is shown in Fig. 1 (b). This aircraft is designed to carry 250 passengers, which makes it slightly larger than an Airbus A321neo aircraft. The aircraft generates thrust through direct hydrogen combustion in two gas turbine engines. Four identical fuel cell systems provide electric power to auxiliary loads such as the environmental control system. During the descent phase, the fuel cells also provide mechanical power to the shafts of the two main engines. This is done to reduce the aircraft's fuel consumption: The engines generally do not generate much thrust during descent, but need to be able to quickly ramp up to full thrust if needed. Maintaining the engines' idle state can consume a considerable amount of hydrogen, especially for short missions. In this concept, the fuel cells power an electric motor that maintains the required temperature- and pressure-level for the main engines [25]. This reduces the aircraft's overall fuel consumption, because the fuel cells operate more efficiently than the gas turbine engines at their idle state. Each of the four fuel cell systems needs to provide an electric base load of 92 kW throughout the mission and an additional 257 kW during the descent phase at an altitude of up to 10670 m. The detailed electric load profile is discussed in Section 4.1.

2.1. Overall fuel cell system layout

The individual fuel cell systems in the two aircraft concepts provide approximately the same maximum power output per system (auxiliary power: 4x 350 kW, propulsion: 10x 312 kW). Hence, the same overall fuel cell system layout is chosen for the two cases. The assumed layout is based on a previous publication [12] and is shown in Fig. 2. The fuel cell system contains three subsystems:

1. Air supply system
2. Stack- and humidification subsystem
3. Thermal management system

The remainder of this section summarizes the key aspects of each subsystem. The air supply system provides pressurized air to the stacks (stream 5) and can potentially recover energy by expanding the stack's exhaust air (stream 4) in a turbine. Several possible topologies for the air supply system are introduced in Section 2.2. The stack- and humidification subsystem combines several fuel cell stacks to achieve the required system-level power output of several hundred kW. Fig. 2 shows an exemplary scenario with two stacks; the actual number of stacks is a result of the system sizing (as described in Section 3.4). Each stack is equipped with a membrane humidifier and a recirculation blower for unconsumed hydrogen.

The thermal management system is used to transfer the system's waste heat to the ambient air. The stack operating temperature is controlled to 85 °C with the bypass of the fuel cell cooler (see Fig. 2). The stacks are operated at their assumed maximum temperature of 85 °C

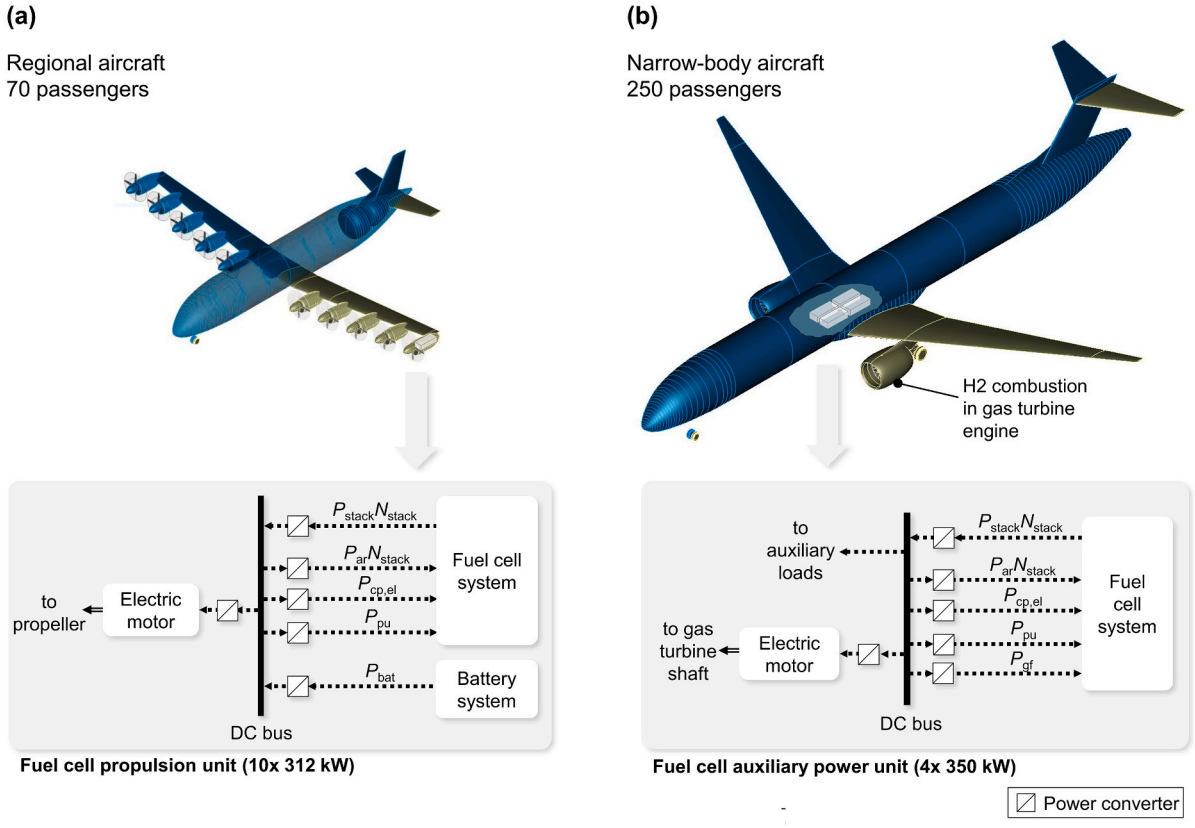

Fig. 1. Investigated aircraft concepts. (a) Regional aircraft with fuel cell based propulsion, based on Refs. [12,24] (b) narrow-body aircraft with fuel cell systems for auxiliary power and assisted idle, based on Ref. [25]. The power flows P_{stack}, P_{ar}, $P_{cp,el}$, P_{pu} and P_{gf} are explained in Section 3.1.

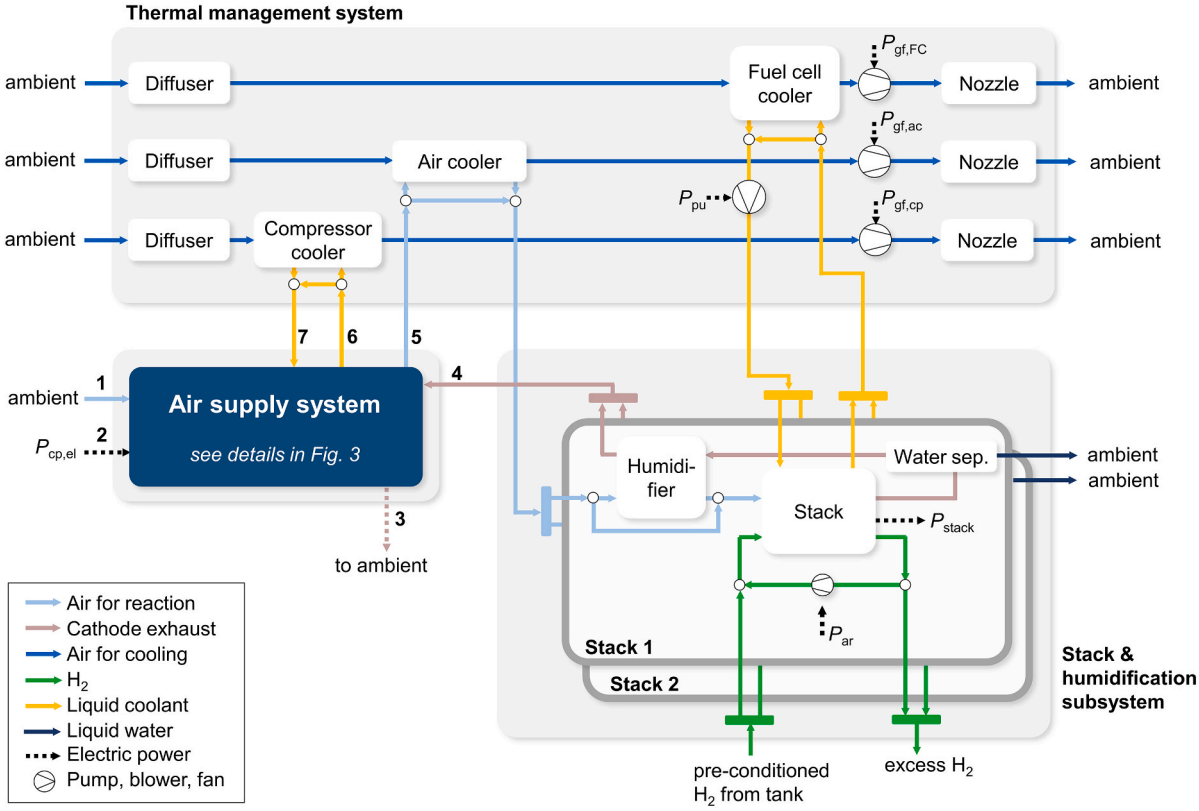

Fig. 2. Investigated fuel cell system layout, based on Ref. [12]. (Water sep. = water separator).

because this minimizes the aerodynamic drag of the thermal management system. A second heat exchanger is used to remove the waste heat of the compressor with a liquid coolant at a temperature of 55 °C. An air-air heat exchanger is used to cool down the hot compressed air (up to 220 °C) to 85 °C before it enters the humidifiers. The stack's cathode exhaust also enters the humidifier at 85 °C and no significant heat transfer occurs in the humidifier. The diffusers reduce the velocity of the incoming ambient air streams and thereby increase the air pressure. If the pressure increase in the diffusers is larger than the pressure drop in the heat exchangers, the thermal management system works passively (i.e., without using the ground fans). For the regional aircraft, the fuel cells are only operated when the aircraft is moving fast enough to allow for passive cooling. A small battery is used for taxiing and takeoff [12]. For the narrow-body aircraft, the fuel cells need to be able to continuously supply the electric base load when the aircraft is on ground. Hence, ground fans are used to enforce an air flow through the heat exchangers when the aircraft is not moving fast enough. Such electrically-driven ground fans are commonly used in the environmental control system of conventional aircraft [28].

In addition to the above subsystems, a hydrogen pre-conditioning system is required to evaporate and heat up the liquid hydrogen from the tanks to the required temperature and pressure at the inlet of the fuel cell's anode recirculation loop (>2.5 bar, >20 °C). The design of such a liquid hydrogen storage and preconditioning system is a separate challenge [29] and is beyond the scope of this work. The two investigated aircraft concepts were designed so that the boiloff rate of the liquid hydrogen tanks is smaller than the aircraft's hydrogen consumption during flight [24,25]. Thus, there is no active cooling required to avoid excessive evaporation of liquid hydrogen during flight.

2.2. Air supply system layout

The air supply system needs to compress the air from a variable ambient pressure (as low as 0.24 bar at 10670 m) to the required pressure at the inlet of the fuel cell stack (>1.0 bar). As explained in the introduction, this can be achieved with a number of different topologies, which are shown in Fig. 3.

The most basic topology only consists of an electrically-driven single-stage radial compressor (see Fig. 3, topology T1). This is a commonly studied topology [8,12,13] that provides reasonable performance with the benefit of a low system complexity. The ambient air (stream 1) enters the air supply system through a diffuser, which reduces the velocity and increases the pressure at the inlet of the compressor. The bypass at the compressor outlet is used for surge control. The surge control of a compressor is necessary to avoid operating points where the required mass flow is too low and would result in flow instabilities [22]. This is achieved by increasing the compressor's air mass flow beyond the required amount and bypassing the excess air to the surroundings (stream 3). This enables a stable compressor operation, but has the drawback of a decreased system efficiency in flight phases where the surge bypass is used [12].

Combining the single-stage compressor with a fixed-geometry turbine leads to topology T2. Such a compressor-turbine-unit is already available for smaller fuel cell systems, but the mass flow of that unit is too low for the investigated aircraft applications [30]. Hence, this work analyzes the potential of this concept based on automotive turbocharger components, which are available for larger mass flows [31]. The specific design of the compressor and turbine stages would need to be modified for aircraft applications, but their overall behavior will be similar. The turbine stage is installed on the same shaft as the compressor and decreases the required motor power. The air that enters the turbine does not contain liquid water because it passes the water separator and membrane humidifier after exiting the stack (see Fig. 2, stream 4). However, the water separator and humidifier alone are not able to avoid condensation inside the turbine under all operating conditions, because the expansion decreases the air temperature. This can lead to

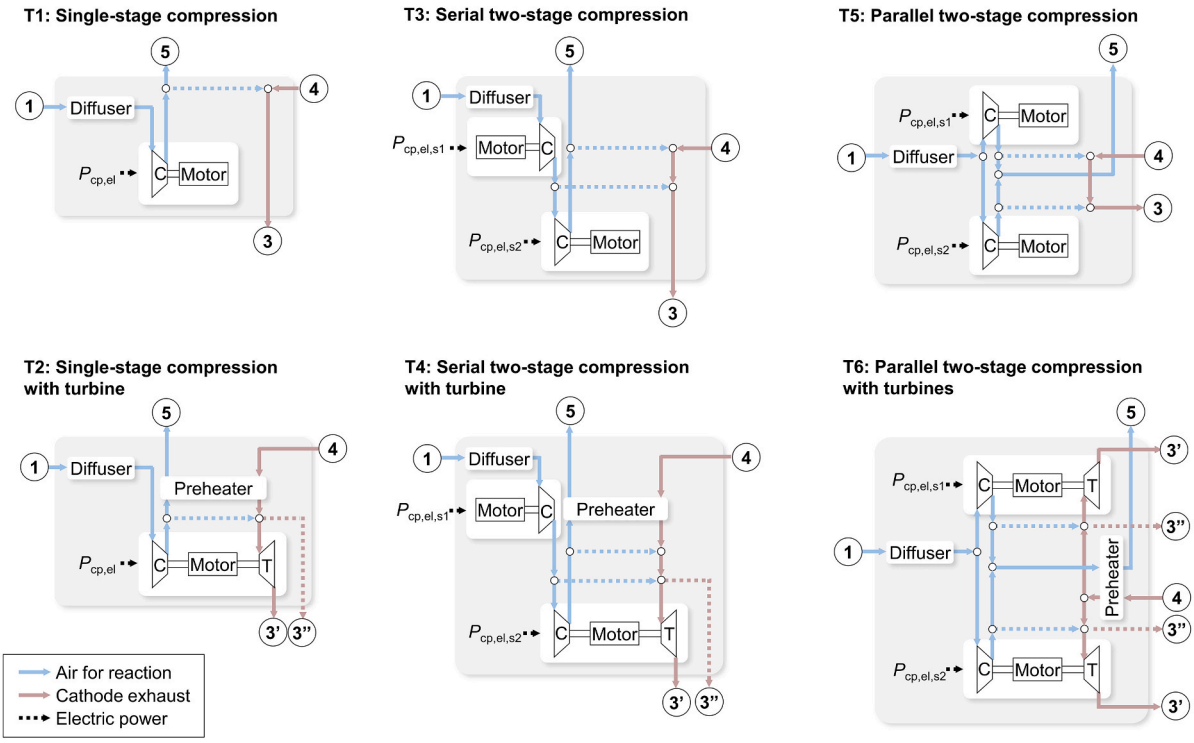

Fig. 3. Investigated topologies of the air supply system (C = compressor stage, T = turbine stage). Valves and the compressor coolant circuit (interfaces 6 and 7) are not shown for simplicity.

condensation of the previously gaseous water content towards the outlet of the turbine stage. The resulting liquid water droplets would decrease the turbine's efficiency and could damage the turbine blades [32,33]. Hence, condensation should be avoided with an appropriate operating strategy. This can be achieved by adding an additional air-air heat exchanger (preheater) and a back-pressure-valve at the turbine outlet [32]. The preheater uses heat from the hot air at the compressor outlet to increase the turbine inlet temperature, which raises the water vapor saturation pressure. If condensation would still occur, the back-pressure-valve at the turbine outlet can be used to reduce the pressure ratio of the turbine (steam 3′). This limits the temperature decrease of the fluid, but results in a reduced power recovery.

Topology T3 adds a second compressor stage to the air supply system. The purpose of using two serial stages is to enable a higher stack operating pressure at low ambient pressures (the pressure ratio of a single stage is typically limited to < 4.5 [31]). The two serial stages could either be placed on the same shaft or on two separate shafts [34,35]. The option with two separate shafts was selected because this enables a better match with the varying air mass flow demand of the fuel cell system. Some applications require a heat exchanger (intercooler) after the first stage to reduce the inlet temperature of the second stage [34]. Because the air temperatures remain moderate within the investigated system (< 220 °C at the outlet of the second stage), the intercooler is omitted. Topology T4 introduces the combination of a serial two-stage compressor with a turbine. The two stages could either be equipped with two turbine stages or the entire energy recovery could take place in a single turbine stage. In the investigated system, the recovered shaft power with a combined turbine was found to be lower than the shaft power of one of the two compressor stages (see Section 4.2). Thus, only one of the compressor stages is equipped with a turbine stage to reduce the system complexity.

Lastly, there is also the option to arrange the two compressor stages in parallel (see Fig. 3, topologies T5 and T6). The benefit of this option is that one of the two stages can be turned off in flight phases with a low air mass flow demand. The two compressor stages are equipped with two separate turbine stages because they will not always be operated at the same time.

3. Thermodynamic system model

An existing model for low-temperature PEM fuel cell systems from an earlier publication [12] is expanded to capture the behavior of different air supply system topologies. The model is implemented in MATLAB. The model inputs are the requirements for the fuel cell system in the respective aircraft (power requirement, altitude, velocity). The model's overall outputs are the fuel cell system's efficiency and aerodynamic drag as well as the system's mass and volume based on an iterative component sizing approach (see Section 3.4). These outputs are calculated for different sets of boundary conditions, which are determined by the respective air supply system topology (see Section 2.2). A flow chart of the thermodynamic system model is shown in Fig. S1 in the supplementary information.

Because the investigated performance indicators (mass, volume, efficiency, drag) refer to steady-state operating points, steady-state models are used. As in most previous aviation-related studies, the aircraft's flight mission is approximated with a number of steady-state operating points [8,16,20]. The model assumes ideal gas behavior and ideal gas mixtures, because the gases in the fuel cell system are present at moderate temperatures and pressures.

The following sections define the system's performance indicators and describe the modeling approach and assumptions for the different air supply system components. This is followed by an explanation of the interfaces to the existing models for the stack, humidifier and thermal management system from Ref. [12]. The flight mission profiles of the two investigated aircraft (i.e., the model inputs) are discussed in Section 4.1.

3.1. Overall system performance indicators

The fuel cell system mass $m_{sys} = \sum m_i$ is approximated based on the

most relevant system components, which are listed in Table 1. The mass of several smaller components such as piping, valves, diffusers and nozzles is assumed to remain constant when using different air supply system topologies. Hence, the mass of these smaller components does not need to be calculated to compare the different topologies. The system volume is approximated analogously based on the volume of the components in Table 1.

The system efficiency $\eta_{\mathrm{sys,LHV}}$ is defined with the effective (net) power output $P_{\mathrm{sys,eff}}$, as well as the mass flow and lower heating value of the consumed hydrogen.

$$\eta_{\mathrm{sys,LHV}} = \frac{P_{\mathrm{sys,eff}}}{\dot{m}_{\mathrm{H_2,sys}} \Delta h_{\mathrm{LHV,H_2}}} \tag{1}$$

The effective power output depends on the power of the stacks P_{stack}, number of stacks N_{stack}, and the power consumption of the auxiliary components $P_{\mathrm{sys,aux}}$.

$$P_{\mathrm{sys,eff}} = N_{\mathrm{stack}} P_{\mathrm{stack}} - P_{\mathrm{sys,aux}} \tag{2}$$

The auxiliary power is defined as

$$P_{\mathrm{sys,aux}} = P_{\mathrm{cp,el}} + N_{\mathrm{stack}} P_{\mathrm{ar}} + P_{\mathrm{pu}} + P_{\mathrm{gf}} \tag{3}$$

with the power flows of the auxiliary components in Table 1. The term $P_{\mathrm{cp,el}}$ describes the compressor's electric power consumption, which depends on the shaft power of the compressor $P_{\mathrm{cp,sh}}$ and the turbine $P_{\mathrm{tb,sh}}$ (see Section 3.2.1). In topologies with two compressor stages, the compressor's overall power consumption is

$$P_{\mathrm{cp,el}} = P_{\mathrm{cp,el,s1}} + P_{\mathrm{cp,el,s2}} \tag{4}$$

where $P_{\mathrm{cp,el,s1}}$ and $P_{\mathrm{cp,el,s2}}$ denote the power consumption of the electric motors of each of the two stages.

The aerodynamic drag of the thermal management system depends on the air supply system topology, because different topologies result in different waste heat flows for the compressor cooler, air cooler and fuel cell cooler. This is considered by calculating the internal drag of the three ram air channels that are used to remove these waste heat flows. The internal drag of each ram air channel is calculated with the cooling air mass flow $\dot{m}_{\mathrm{dr}}$ and the air velocity difference between the inlet of the diffuser and the exit of the nozzle [16].

$$F_d = \dot{m}_{dr}(c_{dr,in} - c_{nz,out}) \tag{5}$$

The total internal drag is

$$F_{d,tot} = F_{d,FC} + F_{d,ac} + F_{d,cp} + F_{d,react} \tag{6}$$

where $F_{\mathrm{d,FC}}$, $F_{\mathrm{d,ac}}$ and $F_{\mathrm{d,cp}}$ correspond to the drag of the fuel cell cooler, air cooler and compressor cooler. The term $F_{\mathrm{d,react}} = \dot{m}_{\mathrm{cp}} c_{\mathrm{dr,in}}$ accounts for the drag that is caused by the stacks' cathode air stream [12].

3.2. Air supply system model

According to the definition in Fig. 2 and Fig. 3, the air supply system consists of the air compressor, turbine and preheater. The modelling approach for these components is described below.

3.2.1. Compressor

The enthalpy change in a compressor stage is [37]

$$\Delta h_{\mathrm{cp}} = \frac{\bar{c}_{\mathrm{p,air}} T_{\mathrm{cp,in}}}{\eta_{\mathrm{cp,s}}} \left(\left(\Pi_{\mathrm{cp}} \right)^{\frac{R_{\mathrm{sp,air}}}{\bar{c}_{\mathrm{p,air}}}} - 1 \right) \tag{7}$$

where $R_{\mathrm{sp,air}}$ is the specific gas constant and $\Pi_{\mathrm{cp}} = p_{\mathrm{cp,out}}/p_{\mathrm{cp,in}}$ is the pressure ratio across the stage. The heat capacity $\bar{c}_{\mathrm{p,air}}$ is the mean value of the temperature-dependent heat capacity between the stage's inlet and outlet temperatures [12]. The compressor's shaft power is

$$P_{\mathrm{cp,sh}} = \Delta h_{\mathrm{cp}} \dot{m}_{\mathrm{cp}} \tag{8}$$

where $\dot{m}_{\mathrm{cp}}$ is the air mass flow. The effective electric power consumption per stage is

$$P_{\mathrm{cp,el}} = \frac{P_{\mathrm{cp,sh}} - P_{\mathrm{tb,sh}}}{\eta_{\mathrm{cp,m}} \eta_{\mathrm{cp,el}} \eta_{\mathrm{cp,pc}}} \tag{9}$$

where $\eta_{\mathrm{cp,m}} = 0.97$ is the mechanical efficiency [38], $\eta_{\mathrm{cp,el}} = 0.94$ is the electric motor efficiency [39] and $\eta_{\mathrm{cp,pc}} = 0.97 \cdot 0.97$ is the overall power converter efficiency (DC/DC and DC/AC) [39]. The power consumption is reduced by the turbine's shaft power $P_{\mathrm{tb,sh}}$ (see section 3.2.2). If there is no turbine, $P_{\mathrm{tb,sh}} = 0$. The mechanical and electric motor losses in the compressor result in a waste heat flow $\dot{Q}_{\mathrm{cp,liq}}$, which is removed with a liquid cooling loop (see Fig. 2).

$$\dot{Q}_{cp,liq} = \Delta h_{cp} \dot{m}_{cp} \left(\frac{1}{\eta_{cp,m} \eta_{cp,el}} - 1 \right) \tag{10}$$

The compressor stage's outlet temperature is calculated with Eq. (11).

$$T_{\mathrm{cp,out}} = \frac{\bar{c}_{\mathrm{p,air}} T_{\mathrm{cp,in}} + \Delta h_{\mathrm{cp}}}{\bar{c}_{\mathrm{p,air}}} \tag{11}$$

The compressor's isentropic efficiency

$$\eta_{\mathrm{cp,s}} = f_{\mathrm{JK}}(\dot{m}_{\mathrm{cp}}, \Pi_{\mathrm{cp}}, c_{i,j,k}) \tag{12}$$

Table 1
Fuel cell system components.

Component	Subsystem in Fig. 2	Power	Mass	Volume	Model description
Compressor	Air supply system	$P_{\mathrm{cp,sh}}$	m_{cp}	V_{cp}	Section 3.2.1
Turbine	Air supply system	$P_{\mathrm{tb,sh}}$	m_{tb}	V_{tb}	Section 3.2.2
Preheater	Air supply system	–	m_{ph}	V_{ph}	Section 3.2.3
Stack	Stack & humidification subsystem	P_{stack}	m_{stack}	V_{stack}	Refs. [12,36]
Humidifier	Stack & humidification subsystem	–	m_{hm}	V_{hm}	Ref. [12]
Anode recirculation blower	Stack & humidification subsystem	P_{ar}	m_{ar}	V_{ar}	Ref. [12]
Ground fans	Thermal management system	P_{gf}	m_{gf}	V_{gf}	See Supplementary information
Fuel cell cooler	Thermal management system	–	$m_{\mathrm{hx,FC}}$	$V_{\mathrm{hx,FC}}$	Ref. [12]
Air cooler	Thermal management system	–	$m_{\mathrm{hx,ac}}$	$V_{\mathrm{hx,ac}}$	Ref. [12]
Compressor cooler	Thermal management system	–	$m_{\mathrm{hx,cp}}$	$V_{\mathrm{hx,cp}}$	Ref. [12]
Coolant pump	Thermal management system	P_{pu}	m_{pu}	V_{pu}	Ref. [12]
Diffusers and nozzles	Thermal management system	–	–	–	Ref. [12]

is evaluated with the semi-empirical Jensen-Kristensen approach [40,41]. The underlying equations for the analytic function f_{JK} in Eq. (12) are described in Ref. [12]. The coefficients $c_{i,j,k}$ of the function f_{JK} are fitted to public manufacturer data for two single-stage compressors: a larger Garrett G42-1200 compressor ($\dot{m}_{cp,max}$ = 0.85 kg/s, $\Pi_{cp,max}$ = 4.2) and a smaller Rotrex C38-91 compressor ($\dot{m}_{cp,max}$ = 0.63 kg/s, $\Pi_{cp,max}$ = 2.9) [31,38]. Details of the parameter fit approach are described in Ref. [12]. The resulting efficiency maps of the two compressors are validated in Fig. 4. Fig. 4 (a) and (c) show the manufacturer data for the two compressors. Note that the G42-1200 compressor achieves a maximum efficiency of 79 % whereas the smaller C38-91 compressor has a maximum efficiency of 75 %. Fig. 4 (b) and (d) show the corresponding result of the model with two different sets of coefficients $c_{i,j,k}$. The simulation result is in good agreement with the manufacturer data.

The depicted compressor maps are also used to determine whether the surge bypass is required in a given operating point. If the stack's required air mass flow $\dot{m}_{cp,req}$ results in a mass flow that is below the surge control limit, then the actually compressed mass flow $\dot{m}_{cp} \geq \dot{m}_{cp,req}$ is increased until the operating point is within the feasible range. The surge control limit is chosen based on the surge line and a 10 % margin for the mass flow [42] (see Fig. 4). The excess mass flow $\dot{m}_{cp,bp}$ is vented to the surroundings or expanded in the turbine.

$$\dot{m}_{cp,bp} = \dot{m}_{cp} - \dot{m}_{cp,req} \tag{13}$$

The effects of different inlet pressures $p_{cp,in}$ and temperatures $T_{cp,in}$ on the compressor map are considered with the Mach number similarity approach [41,43,44]. The corrected mass flow $\dot{m}_{cp,red}$ is given by Eq. (14).

$$\dot{m}_{cp,red} = \dot{m}_{cp}\frac{p_{ref}}{p_{cp,in}}\sqrt{\frac{T_{cp,in}}{T_{ref}}} \tag{14}$$

Different compressor sizes (i.e., different $\dot{m}_{cp,max}$ and $\Pi_{cp,max}$) are considered by using normalized compressor efficiency maps. The two compressor maps in Fig. 4 (b) and (d) are normalized with respect to their point of maximum efficiency $\eta_{cp,s,max}$ based on Eqs. (15) and (16).

$$\dot{m}_{cp,norm} = \frac{\dot{m}_{cp,red}}{\left(\dot{m}_{cp,red}\right)_{\eta_{cp,s,max}}} \tag{15}$$

$$\Pi_{cp,norm} = \frac{\Pi_{cp}}{\left(\Pi_{cp}\right)_{\eta_{cp,s,max}}} \tag{16}$$

To represent the efficiency maps of geometrically similar compressors with a different size, these normalized maps are scaled to a different $\dot{m}_{cp,max}$ and $\Pi_{cp,max}$. The background and validation of this empirical scaling approach are described in Ref. [12]. The scaled efficiency map of the C38-91 compressor is used if the required maximum pressure ratio $\Pi_{cp,max}$ is $\leq$ 3.4. For $\Pi_{cp,max}$ > 3.4, the scaled map of the larger G42-1200 compressor is used.

The behavior of a single-stage compressor is described by Eqs. (7)–(16). In this case, the required pressure ratio per stage is >3.4 and the normalized efficiency map of the G42-1200 compressor is scaled according to Eqs. (15) and (16). If there are two serial compressor stages, Eqs. (7)–(16) are applied for each stage and the inlet conditions of the second stage are determined by the outlet conditions of the first stage. The overall pressure ratio Π_{cp} is the product of the two individual pressure ratios. Both stages are designed to contribute equally to the overall pressure ratio, so that $\Pi_{cp,s1} = \Pi_{cp,s2} = \sqrt{\Pi_{cp}}$ (s1 denotes stage 1, s2 denotes stage 2). With two serial stages, the required pressure ratio per stage is < 3.4 and the normalized map of the C38-91 compressor is scaled to the respective requirements of each stage according to Eqs. (15) and (16).

If there are two parallel compressor stages, both stages provide the same pressure ratio $\Pi_{cp,s1} = \Pi_{cp,s2} = \Pi_{cp}$ and different mass flows. Their

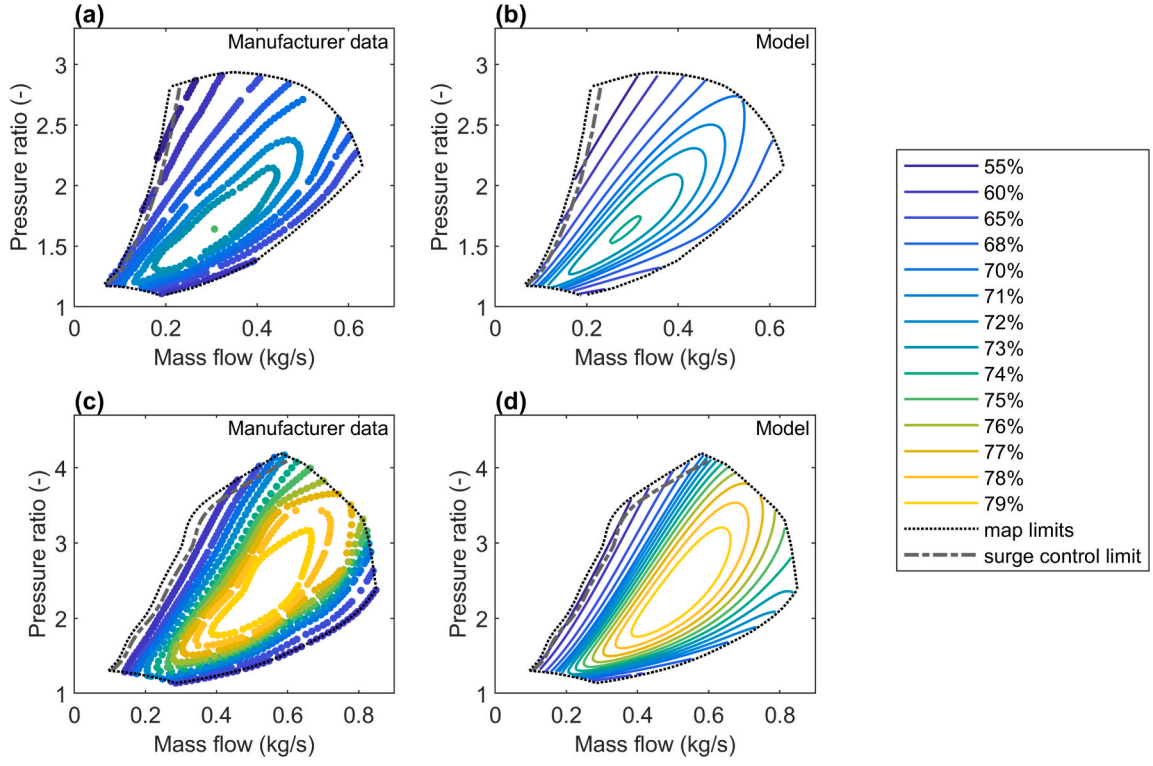

Fig. 4. Efficiency of the investigated compressors for different mass flows $\dot{m}_{cp,red}$ and pressure ratios Π_{cp} (reference conditions: 15 °C, 1.013 bar). (a) Manufacturer data: Rotrex C38-91 compressor [38] (b) Empirical model: Rotrex C38-91 compressor, from Ref. [12] (c) Manufacturer data: Garrett G42-1200 compressor [31] (d) Empirical model: Garrett G42-1200 compressor.

share of the overall air mass flow is described by the ratio r_{mf}.

$$\dot{m}_{cp,s1} = r_{mf}\dot{m}_{cp} \tag{17}$$

$$\dot{m}_{cp,s2} = (1 - r_{mf})\dot{m}_{cp} \tag{18}$$

When sizing the system, r_{mf} is set to a fixed value (0.5 for regional aircraft, 0.25 for narrow-body aircraft). When simulating a previously sized system, r_{mf} is numerically optimized to find the split that results in the lowest overall power consumption of the two stages. In the case of two parallel stages, the required pressure ratio per stage is > 3.4. Hence, the normalized efficiency map of the G42-1200 compressor is scaled to the respective requirements of each stage according to Eqs. (15) and (16).

The overall mass and volume of each compressor stage consist of the mechanical components (impeller and housing), the electric motor and the power converter. The mass and volume of the mechanical components is calculated by linearly scaling the mass and volume of a baseline design (6.0 kg, 4.0 L, $\dot{m}_{cp,max}$= 0.63 kg/s [38]) with the compressor's maximum mass flow. The mass and volume of the electric motor and power converter are calculated by linearly scaling the compressor's maximum power consumption P_{cp} with the specific power and power density of a baseline design (electric motor: 1.34 kW/kg and 1.77 kW/L, power converter: 6.03 kW/kg and 4.51 kW/L) [45].

3.2.2. Turbine

The enthalpy change in a turbine stage is [37]

$$\Delta h_{tb} = \eta_{tb,s} c_{p,air} T_{tb,in}\left(1 - \left(\frac{1}{\Pi_{tb}}\right)^{\frac{R_{sp,air}}{c_{p,air}}}\right) \tag{19}$$

where $\Pi_{tb} = p_{tb,in}/p_{tb,out}$ is the turbine's pressure ratio. The specific heat capacity $c_{p,air}$ is evaluated at the turbine inlet temperature $T_{tb,in}$. The shaft power of the turbine is

$$P_{tb,sh} = \Delta h_{tb}\dot{m}_{tb} \tag{20}$$

where $\dot{m}_{tb}$ is the air mass flow that is expanded in the turbine. For a given pressure ratio, a fixed-geometry turbine can only operate at a narrow range of mass flows [46]. If the mass flow at the turbine inlet is too high, part of it needs to be bypassed to the surroundings. If the mass flow is too low, all of the air is bypassed and the turbine cannot reduce the compressor power in that flight phase. Fig. 5 (a) shows feasible combinations of mass flow and pressure ratio for several fixed-geometry turbines (public manufacturer data from Ref. [31]). Note that the curves show the mean mass flow for a given pressure ratio and do not explicitly consider the variation of the rotational speed. In a more detailed turbine map, each mass flow corresponds to a limited range of rotational speeds [47]. However, such detailed data is not publicly available for the investigated turbines and is not required for the chosen modeling approach. Fig. 5 (b) shows the same curves in terms of normalized mass flow $\dot{m}_{tb,norm}$ and pressure ratio $\Pi_{tb,norm}$ according to the definitions in Eqs. (21) and (22).

$$\dot{m}_{tb,norm} = \frac{\dot{m}_{tb,red}}{\dot{m}_{tb,max}} \tag{21}$$

$$\Pi_{tb,norm} = \frac{\Pi_{tb} - 1}{\Pi_{tb,max} - 1} \tag{22}$$

It is found that all these turbines can approximately be described by the same normalized function $\dot{m}_{tb,norm} = f_{tb}(\Pi_{tb,norm})$. Therefore, this normalized function f_{tb} can also be used to approximate the behavior of geometrically similar turbines with different sizes (within the validated range). The normalized function is implemented as a lookup table. The datapoints of the lookup table are obtained by normalizing public manufacturer data for a Garrett G42 turbine from Ref. [31] with Eqs. (21) and (22). When sizing a turbine stage for a given topology, $\dot{m}_{tb,max}$ and $\Pi_{tb,max}$ are chosen based on the maximum mass flow and pressure ratio that the turbine encounters.

When simulating a previously sized turbine, the scaled function f_{tb} is used to determine the usable mass flow $\dot{m}_{tb} \leq \dot{m}_{tb,av}$ for a given pressure ratio Π_{tb} and available mass flow $\dot{m}_{tb,av}$. The excess mass flow $\dot{m}_{tb,bp}$ is bypassed to the surroundings.

$$\dot{m}_{tb} = \dot{m}_{tb,av} - \dot{m}_{tb,bp} \tag{23}$$

Analogously to the compressor model, the effects of different inlet pressures $p_{tb,in}$ and temperatures $T_{tb,in}$ are considered with the Mach number similarity approach [41,43]. The corrected turbine mass flow $\dot{m}_{tb,red}$ is given by Eq. (24).

$$\dot{m}_{tb,red} = \dot{m}_{tb}\frac{p_{ref}}{p_{tb,in}}\sqrt{\frac{T_{tb,in}}{T_{ref}}} \tag{24}$$

The datasheet of the investigated Garrett G42 turbine only states the maximum turbine efficiency of 77 % [31]. Bozza and De Bellis [47] showed that the efficiency of radial fixed-geometry turbines typically varies by about 10 % across the operating range. Hence, the isentropic turbine efficiency $\eta_{tb,s}$ is set to 67 % as a conservative assumption.

The temperature and relative humidity at the turbine outlet are given by

$$T_{tb,out} = T_{tb,in} - \frac{\Delta h_{tb}}{c_{p,air}} \tag{25}$$

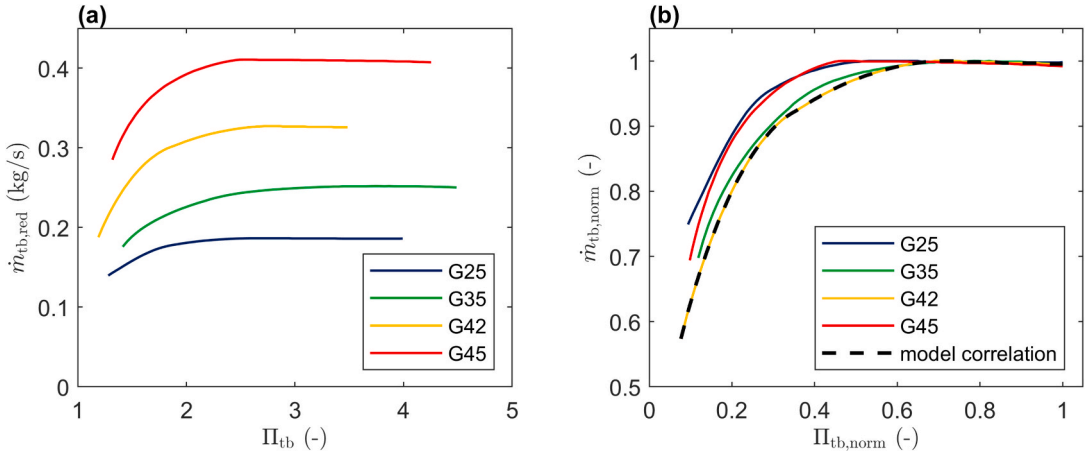

Fig. 5. Feasible operating points of fixed-geometry turbines (reference conditions: 15 °C, 1.013 bar). (a) Manufacturer data for four different turbine stages: Garrett G25, Garrett G35, Garrett G42, Garrett G45 [31] (b) Normalized curves for the same four turbines.

$$RH_{\mathrm{tb,out}} = \frac{X_{\mathrm{H2O,tb}} p_{\mathrm{tb,out}}}{p_{\mathrm{sat}}} \tag{26}$$

where $X_{\mathrm{H2O,tb}}$ is the molar fraction of water and $p_{\mathrm{sat}}(T_{\mathrm{tb,out}})$ is the saturation vapor pressure. $X_{\mathrm{H2O,tb}}$ is calculated based on the known composition of the air streams from the humidifier (see Section 3.3) and the compressor's surge bypass. As discussed in Section 2.2, condensation in the turbine should be avoided at all times. The model considers this as follows: The preheater model determines the turbine inlet temperature $T_{\mathrm{tb,in}}$ (see Section 3.2.3). The resulting $T_{\mathrm{tb,out}}$ and $RH_{\mathrm{tb,out}}$ are calculated with Eqs. (25) and (26). If the temperature increase in the preheater is not sufficient to achieve $RH_{\mathrm{tb,out}} \leq 1$, then the outlet pressure $p_{\mathrm{tb,out}}$ is raised iteratively until $RH_{\mathrm{tb,out}} \leq 1$ is achieved. The resulting loss in the turbine's shaft power is calculated with Eq. (19).

The mass and volume of the turbine stage are calculated with a linear scaling law based on the turbine's maximum mass flow $\dot{m}_{\mathrm{tb,max}}$.

$$m_{\mathrm{tb}} = s_{\mathrm{tb,m}} \dot{m}_{\mathrm{tb,max}} \tag{27}$$

$$V_{\mathrm{tb}} = s_{\mathrm{tb,V}} \dot{m}_{\mathrm{tb,max}} \tag{28}$$

The mass of a turbine stage is typically not published by manufacturers. Therefore, the scaling factors are approximated as $s_{\mathrm{tb,m}} = 9.52\,\mathrm{kg/(kg/s)}$ and $s_{\mathrm{tb,V}} = 0.0063\,\mathrm{m^3/(kg/s)}$ based on the mechanical components of the compressor stage (see Section 3.2.1). This approach can be justified with manufacturer data for the Fischer EMTC compressor series [30], which states that the version with two compressor stages (EMTCC-120k) has approximately the same mass as the version with one compressor stage and one turbine stage (EMTCT-120k).

3.2.3. Preheater

The preheater model considers an air-air heat exchanger with louvered-fin surfaces. Details of the heat exchanger model are described in a previous publication [12]. The remainder of this section explains how the existing heat exchanger model is used to size and simulate the preheater in the air supply system. The mass flow, temperature and pressure of the two air streams at the inlets of the preheater are known from the compressor model (hot stream) and humidifier model (cold stream). The preheater model is used to determine the required heat exchanger size to achieve the desired outlet temperature of the cold air stream $T_{\mathrm{ph,c,out}}$. The target for $T_{\mathrm{ph,c,out}}$ is set to 120 °C to avoid condensation in the turbine. The cold stream inlet temperature remains constant at 85 °C (from humidifier). The heat exchanger is sized in a non-linear optimization problem, which considers a large number of possible fin arrangements and selects the lightest design that meets the sizing constraints [12]. The sizing constraints are given by the desired outlet temperature $T_{\mathrm{ph,c,out}}$ and the pressure drops of the hot and cold air streams, which are chosen as $\Delta p_{\mathrm{ph,h}} \leq 5000\,\mathrm{Pa}$ and $\Delta p_{\mathrm{ph,c}} \leq 5000\,\mathrm{Pa}$. The results of the non-linear optimization problem are the preheater mass m_{ph} and volume V_{ph} at the optimal solution (i.e., the optimal fin arrangement for the preheater). When simulating a previously sized heat exchanger, only the inlet conditions of the hot and cold air streams are known. In this case, the model is solved numerically for the transferred heat flow as well as the outlet temperatures and the pressure drops of the hot and cold air streams.

3.3. Interfaces with existing component models

Each of the different air supply system topologies has the same interfaces to the other parts of the fuel cell system. These interfaces are numbered as 1…7 in Fig. 2 and are summarized in Table 2. Note that for interface 1, the ambient temperature from the international standard atmosphere is increased by an offset of 22.8 °C to resemble a "hot day" scenario (37.8 °C at sea level) [48]. The "hot day" scenario is chosen because it is the most challenging ambient condition for the thermal management system and the compressor [12].

Table 2
Interfaces between the air supply system and the overall fuel cell system. The numbers of the interfaces refer to those in Fig. 2.

Interface	Description	Symbol	Value/Background
1	Ambient air flow into compressor	$\dot{m}_{\mathrm{cp}}$	Eq. (13)
1	Ambient air pressure	p_{amb}	Interpolated from International Standard Atmosphere [49]
1	Ambient air temperature	T_{amb}	Interpolated from International Standard Atmosphere [49]
2	Compressor electric power consumption	$P_{\mathrm{cp,el}}$	Eqs. (4) and (9)
3	Oxygen-depleted air that is vented to the surroundings (after turbine/ humidifier/ compressor surge bypass)	$\dot{m}_{\mathrm{vent}}$	See Table S1 in supplementary information
4	Humid oxygen-depleted air from wet side of membrane humidifier	$\dot{m}_{\mathrm{hm,w,out}}$	Known from humidifier model [12]
5	Compressed air flow after compressor	$\dot{m}_{\mathrm{cp,req}}$	Known from stack model [12]
6	Coolant mass flow at outlet of compressor unit	$\dot{m}_{\mathrm{ccp,out}}$	Calculated from $\dot{Q}_{\mathrm{cp,liq}}$ from Eq. (10)
6	Coolant temperature at outlet of compressor unit	$T_{\mathrm{ccp,out}}$	55 °C [12]
7	Coolant mass flow at inlet of compressor unit	$\dot{m}_{\mathrm{ccp,in}}$	$\dot{m}_{\mathrm{ccp,in}} = \dot{m}_{\mathrm{ccp,out}}$
7	Coolant temperature at inlet of compressor unit	$T_{\mathrm{ccp,in}}$	50 °C [12]

3.4. Fuel cell system sizing

The required size of each fuel cell system component is determined with an iterative sizing approach, which is described in detail in Ref. [12]. Briefly summarized, the approach determines the smallest feasible combination of fuel cell system components that is required to meet the aircraft's electric load demand. The size of the fuel cell stacks, compressor, humidifier, coolant pump, anode recirculation blower, heat exchangers, diffusers and nozzles are varied numerically until convergence is achieved. The stack operating conditions (pressure and relative humidity at the cathode inlet) are optimized for each flight phase in order to maximize the system efficiency. The optimization considers the contradicting effects of an increased operating pressure for the stacks: higher pressures improve the stack's cell voltage and efficiency, but increase the auxiliary power consumption of the compressor. The effect of varying operating pressures on the stack's cell voltage and efficiency is considered with a validated 1D fuel cell stack model from our previous publication [12]. The stack model output for different currents, pressures and relative humidities is shown in Fig. S2 in the supplementary information. As described in Ref. [12], the stack model is also used to capture the effect of different compressor pressure ratios on the required stack size by adjusting the number of cells based on the stack's power output at different pressures. The iterative sizing approach also considers the varying air mass flow demand and waste heat of the stack at different operating pressures, which affects the size of the remaining auxiliary components (humidifier, thermal management, etc.). The feasible operating range of the compressor (see Section 3.2.1) is considered as a constraint when optimizing the stack pressure. This ensures that only feasible compressor operating points (i.e., points within the map limits) are considered. The stack's cathode stoichiometric ratio is kept constant at the assumed feasible minimum of 1.7 to minimize the air flow that needs to be supplied by the compressor. To account for the different air supply system topologies, several modifications were made to the original iterative sizing approach from Ref. [12]. These modifications are described in the supplementary

information.

3.5. Model validation and accuracy

The component models for the compressor and turbine are validated in Fig. 4 and Fig. 5 by comparing the model output to manufacturer data for different mass flows and pressure ratios. The assumed linear correlation for the compressor and turbine mass is based on manufacturer specifications, but could not be validated for different compressor and turbine types because of the lack of detailed public data on the mass of such components. However, because the compressor and turbine mass is rather small compared to the mass of the remaining fuel cell system components (see results in Section 4.2), this does not introduce a significant inaccuracy for the overall results. The assumption of a constant turbine efficiency is a simplification, but a sensitivity study on this parameter showed that the model results are relatively robust with respect to this assumption (see Section 4.2). The validation and accuracy of the remaining component models for the stack, humidifier, heat exchangers, coolant pump, anode recirculation blower, diffusers and nozzles is discussed in detail in our previous publication [12].

4. Results and discussion

4.1. Mission profiles

The fuel cell system model is used to assess the performance of the six investigated air supply system topologies for each of the two aircraft concepts. The design mission of the regional aircraft with fuel cell-based propulsion is shown in Fig. 6 (a) to (c). The highest power requirement of 10x 312 kW occurs during takeoff (TO). The climb phase (CL) and cruise phase (CR) require somewhat less electric power, followed by a very low power demand during the descent phase (DE). The design mission of the narrow-body aircraft is shown in Fig. 6 (d) to (f). In that case, the fuel cells only provide an electric auxiliary load of 4x 92 kW throughout most of the mission. As described in section 2, the fuel cells are used to maintain the rotational speed of the aircraft's two main engines during descent. This results in an increased electric load demand of 4x 349 kW throughout the descent phase.

4.2. Optimal topology for regional aircraft propulsion

This section investigates how different air supply system topologies affect the overall fuel cell system performance in the regional aircraft. The topologies are compared in terms of mass, efficiency and drag, because these are the most critical performance indicators for an aircraft propulsion system [50]. The results for the volume of the fuel cell system are used to check whether the overall volume (including tank and fuel) remains within a reasonable range. The iterative sizing process is used to identify the smallest feasible combination of component sizes that can provide the aircraft's electric load demand (see Section 3.4). This process is repeated for each of the six investigated topologies. The sizing is conducted for 7 steady-state points that are shown in Fig. 6 (a) to (c). After the sizing is complete, the fully sized system is simulated with a higher temporal resolution of 25 steady-state points.

The results of the system sizing for the regional aircraft are shown in Fig. 7 (a) to (c). The components of the baseline topology T1 (single stage compressor, no turbine) are predicted to weigh 421.9 kg (see Fig. 7 (a)). This results in a specific power of 0.74 kW/kg (excluding the tank), which is higher than the manufacturer specifications for an existing fuel cell system by Powercell (0.47 kW/kg) [15]. This is expected, since the model considers a larger compressor with a maximum efficiency of 79 % (Garrett G42, see Section 3.2.1). Moreover, the simulated value does not include the mass of valves, tubes, wiring and structural components (see Section 3.1). The consumed hydrogen mass in one of the ten fuel cell systems is found to be 56.9 kg. In combination with a LH2 tank gravimetric efficiency of 25 % [4], this leads to a LH2 tank mass of 227.5 kg per fuel cell system. The resulting total LH2 tank mass is 2275 kg (excluding reserves).

An added turbine (topology T2) is predicted to decrease the overall mass by 4.5 %. To expand the fuel cell exhaust in a turbine stage without the risk of water condensation, the air needs to be heated in an additional heat exchanger (preheater). Nonetheless, the energy recovery benefits of a turbine stage are found to outweigh the mass of the turbine stage (1.9 kg) and preheater (2.3 kg) by far. The use of a serial two-stage

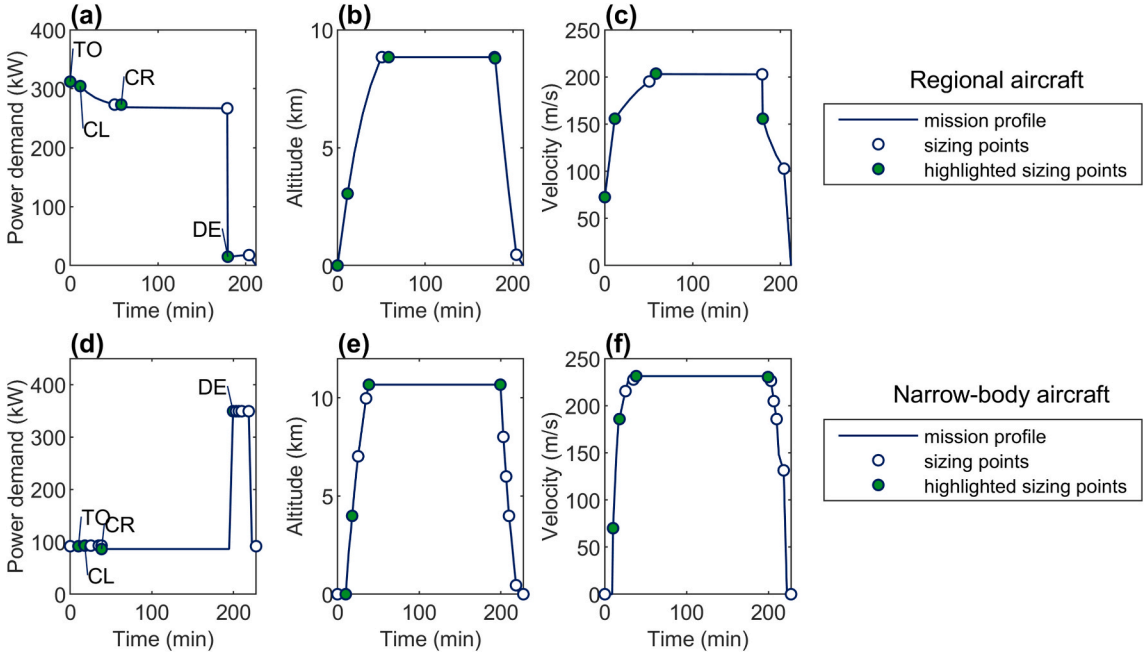

Fig. 6. Mission profiles of the two investigated aircraft concepts [12,24,25] (a) regional aircraft: electric power demand for one of the ten fuel cell systems (b) regional aircraft: altitude (c) regional aircraft: velocity (d) narrow-body aircraft: electric power demand for one of the four fuel cell systems (e) narrow-body aircraft: altitude (f) narrow-body aircraft: velocity.

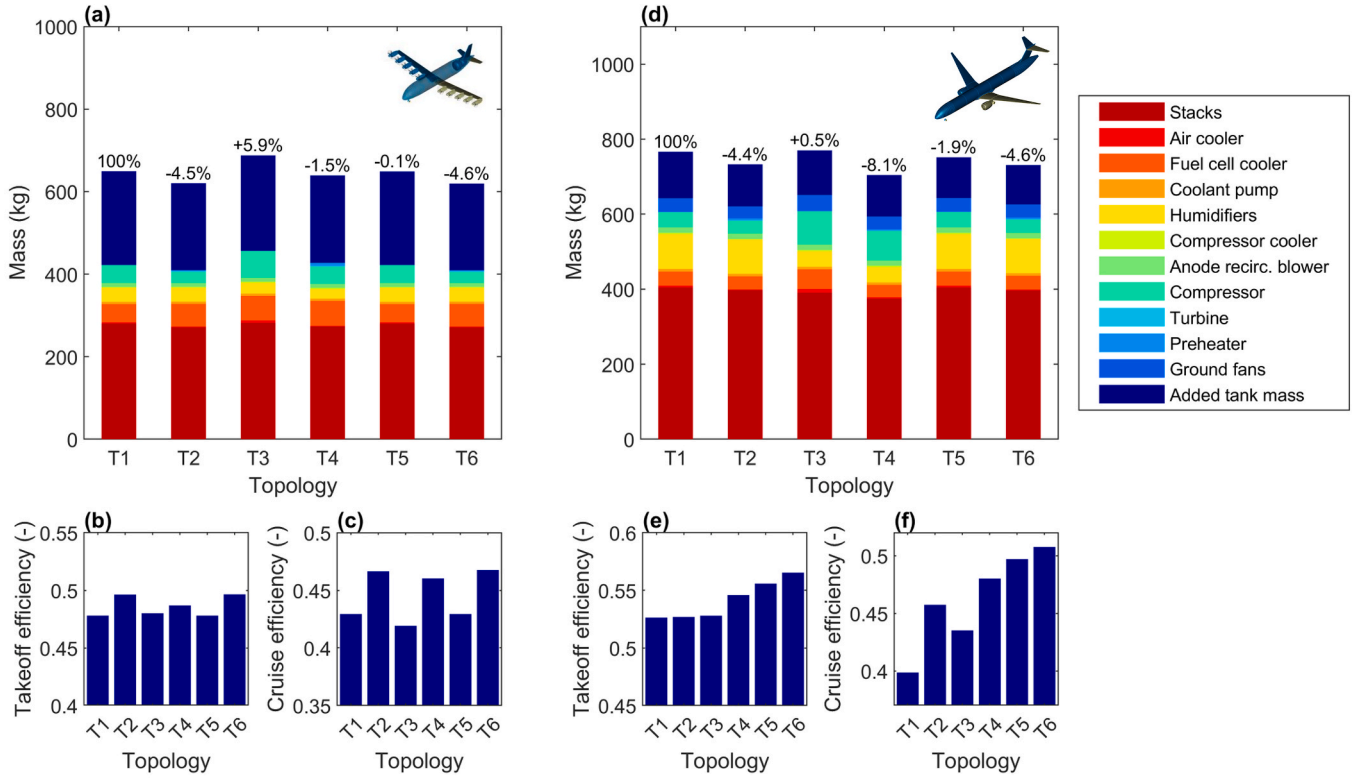

Fig. 7. Optimal air supply system topology for regional aircraft propulsion (a)-(c) and auxiliary power supply in narrow-body aircraft (d)-(f). The topologies T1-T6 are defined in Fig. 3. The figure shows the component mass for one of the fuel cell systems (the regional aircraft contains 10 systems, the narrow-body aircraft contains 4 systems). (a) Propulsion: component mass, (b) propulsion: system efficiency during takeoff, (c) propulsion: system efficiency during cruise, (d) auxiliary power: component mass, (e) auxiliary power: system efficiency during takeoff, (f) auxiliary power: system efficiency during cruise. Aircraft images reproduced from Refs. [24,25].

compressor is predicted to result in a mass increase of 5.9 % without a turbine (T3) and a slight decrease by 1.5 % with a turbine (T4). The parallel two-stage compressor topologies with and without a turbine (T5 and T6) result in a similar overall mass as the respective single-stage topologies. The overall volume is found to be in a feasible range for all topologies and varies by −6.4 % to + 2.3 % compared to the baseline (see supplementary information).

The different tank sizes in Fig. 7 (a) can be explained with the efficiency of the different topologies. The overall fuel cell system efficiency during takeoff and cruise is compared in Fig. 7 (b) and Fig. 7 (c). All topologies with a turbine (T2, T4, T6) can improve the system efficiency during takeoff and cruise. However, topologies T4 and T6 lead to slightly higher efficiencies during takeoff. The aerodynamic drag with the different topologies is shown in the supplementary information. Most topologies lead to a slight increase compared to the baseline topology T1. However, this increase in drag is negligibly small compared to the aircraft's thrust and is therefore assumed to not affect the selection of the optimal topology (see supplementary information).

The improved performance of topologies T2 and T6 can be explained with a more detailed analysis of the power flows in the fuel cell system. Fig. 8 (a) shows the overall system efficiency throughout the entire flight mission for topology T2. The highlighted points TO, CL, CR and DE correspond to the four phases takeoff, climb, cruise and descent. The corresponding net system power $P_{sys,eff}$, stack power $P_{stack}N_{stack}$ and auxiliary power $P_{sys,aux}$ are shown in Fig. 8 (c). The main contributors to the auxiliary power are the compressor (increases $P_{sys,aux}$) and the turbine (decreases $P_{sys,aux}$). The shaft power of these two components is shown in more detail in Fig. 8 (e). The turbine reduces the required compressor power $P_{cp,el}$ by 40–49 % during takeoff, climb and cruise. During descent, the air flow is too low to operate the turbine and $P_{tb,sh} = 0$. The corresponding stack operating pressure and ambient pressure are shown in Fig. 8 (g). The stack pressure is optimized for each flight phase to maximize the efficiency (see Section 3.4).

With topology T6, the efficiency follows a similar pattern throughout most of the flight mission but is significantly higher during the descent phase (see Fig. 8 (b), point "DE"). This can be explained with the surge control of the compressors. The low electric power requirement during the descent phase results in a low air mass flow requirement for the compressor (see point "descent req." in Fig. 8 (i)). The single-stage compressor in topology T2 needs to compress considerably more air than what is required by the stack to move the operating point beyond the surge line (see point "descent act." in Fig. 8 (i)). The two parallel compressor stages in topology T6 are designed to operate simultaneously during takeoff, climb and cruise. During descent, only stage 1 is used and stage 2 is bypassed. This results in a smaller surge bypass flow and a lower compressor power consumption during the descent phase (see Fig. 8 (j)). The temperature range of the main fluid streams in the air supply system as well as detailed results for the other topologies are included in the supplementary information.

In summary, topologies T2 and T6 are both able to improve the efficiency and overall system mass compared to the baseline (topology T1). Topology T6 further improves the efficiency during descent. However, the overall mass including the tank is nearly the same for both topologies because the descent phase only lasts for a short time. Considering that topology T6 is significantly more complex, it can be concluded that topology T2 (single-stage compressor with turbine) is the best option for the investigated regional aircraft.

The above analysis is based on assumptions for the turbine efficiency $\eta_{tb,s}$ (constant, see Section 3.2.2) and compressor efficiency $\eta_{cp,s}$ (based on compressor map, see Section 3.2.1). Fig. 9 explores the effect of different efficiency assumptions on the turbine power share $P_{tb,sh}/P_{cp,sh}$ during the cruise phase of the regional aircraft (topology T2, point "CR"

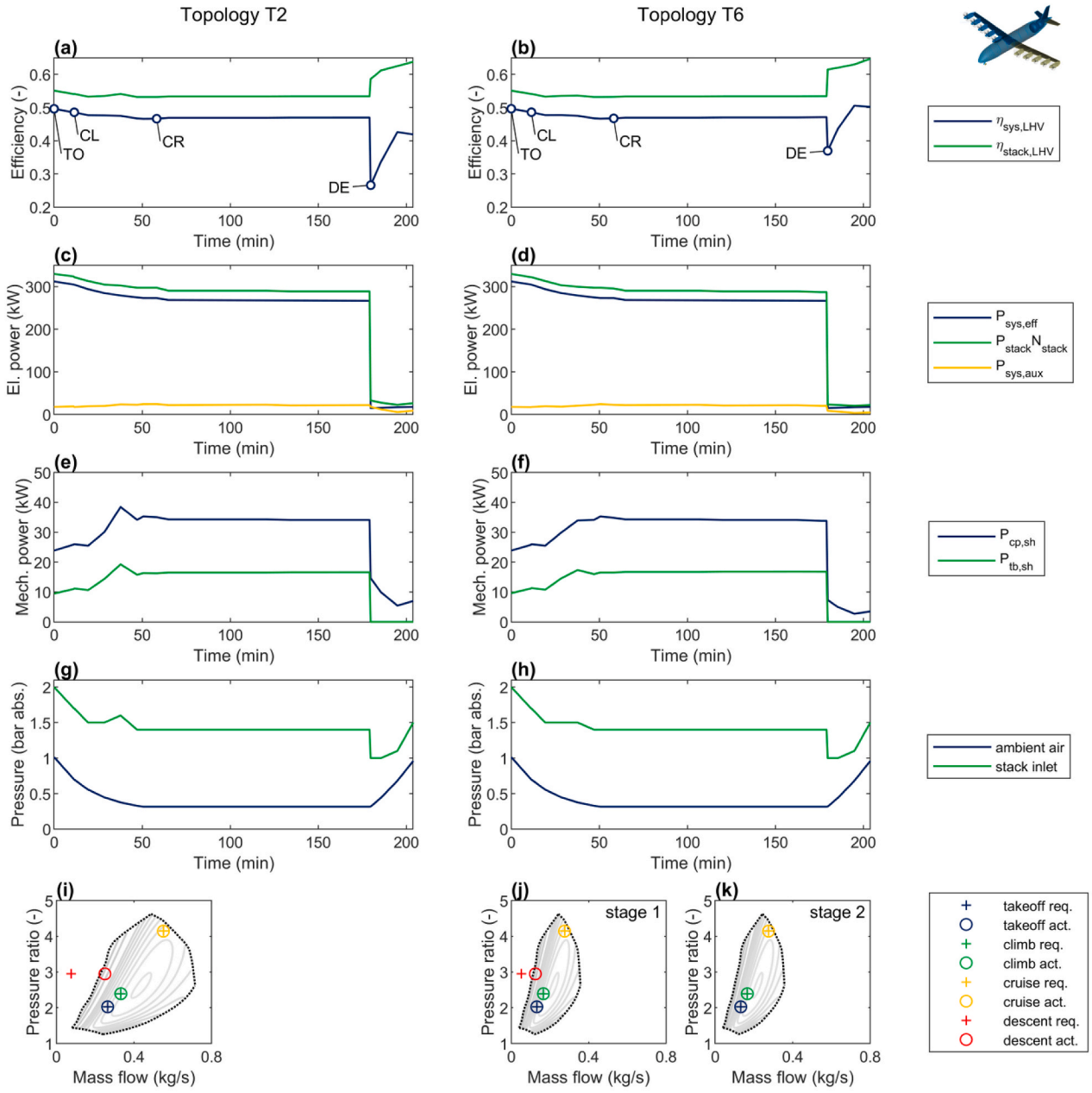

Fig. 8. Air supply system topologies for regional aircraft propulsion: detailed results for topology T2 (left) and T6 (right). The figure shows results for one of the aircraft's ten identical fuel cell systems. (a) and (b): system efficiency $\eta_{sys,LHV}$ and stack efficiency $\eta_{stack,LHV}$, (c) and (d): electrical power, (e) and (f): mechanical shaft power, (g) and (h): pressures, (i) to (k): compressor maps (req.: air mass flow that is required by the stacks, act: actual compressed mass flow). Aircraft image reproduced from Ref. [24].

in Fig. 8 (a)). The overall system model assumes $\eta_{tb,s} = 0.67$ and $\eta_{cp,s} = 0.77$ for this operating point. These assumptions result in a turbine power share of 47 % (see circle in Fig. 9 (a)). As expected, lower turbine efficiencies would lead to a lower turbine power share. However, an increased turbine efficiency would also lead to a decreased turbine power share in this operating point. This unintuitive effect occurs because of the constraint to avoid condensation at the turbine outlet. Higher turbine efficiencies lead to an increased enthalpy change and a reduced turbine outlet temperature (see Eqs. (19) and (25)). To prevent condensation, the pressure ratio of the turbine is reduced with a valve at the turbine outlet if the relative humidity at the turbine outlet would exceed a value of one (see section 3.2.2). In this operating point, increased turbine efficiencies would require a reduction of the pressure ratio $\Pi_{tb} = p_{tb,in}/p_{tb,out}$, which reduces the shaft power of the turbine (see Fig. 9 (d) and (g)). Increased compressor efficiencies would lead to a similar effect but slightly higher turbine power shares (see Fig. 9 (b) and (c)).

4.3. Optimal topology for auxiliary power supply in narrow-body aircraft

Next, we investigate how a different mission profile can change the choice of the best air supply system topology. To do this, the iterative component sizing is repeated for the case where the fuel cell system provides auxiliary power in the larger narrow-body aircraft. The results for the system mass in this aircraft concept are shown in Fig. 7 (d). Here, an added turbine (T2) can reduce the overall system mass by 4.4 % compared to the baseline (T1). The use of a serial two-stage compressor in combination with a turbine (T4) leads to an even higher mass

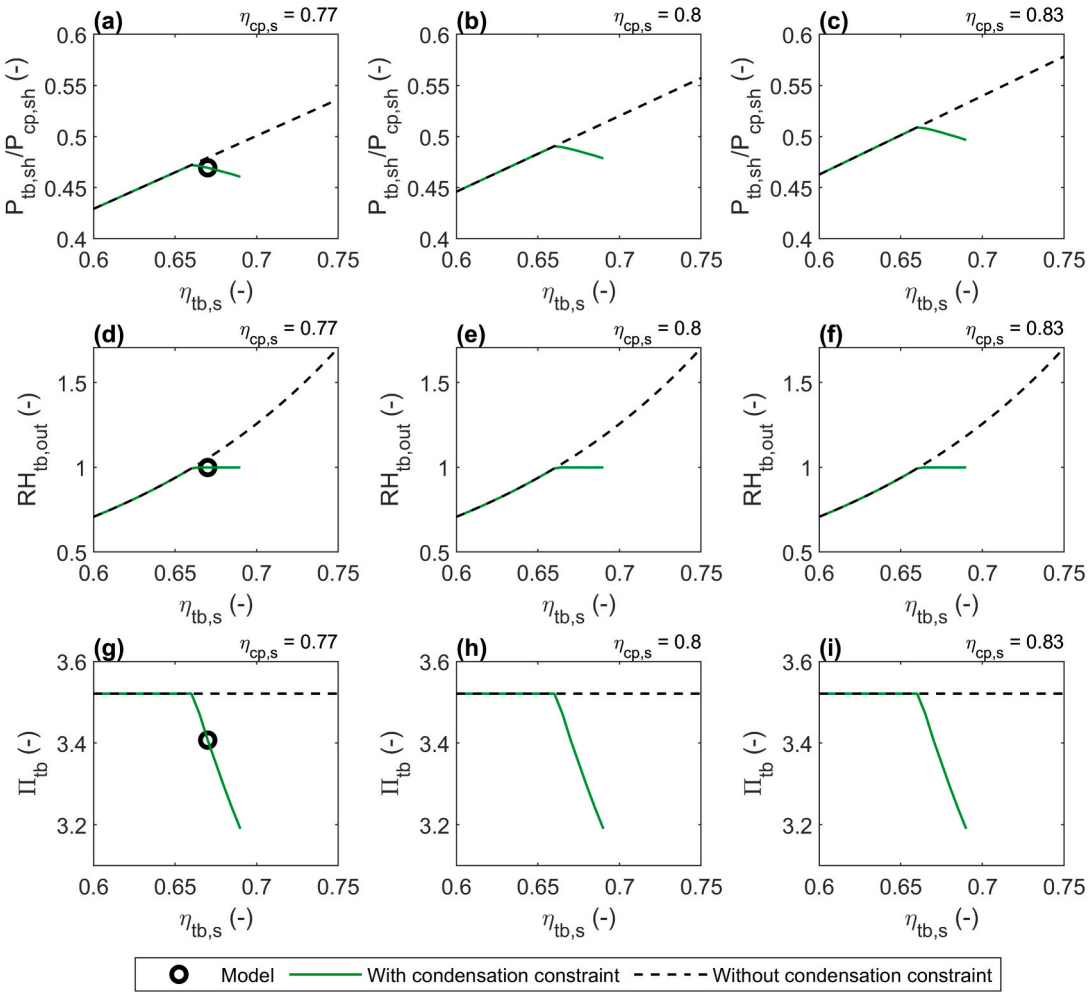

Fig. 9. Effect of different assumptions for the turbine efficiency $\eta_{tb,s}$ and compressor efficiency $\eta_{cp,s}$ on the turbine behavior in the cruise phase of the regional aircraft concept (values for topology T2). (a) to (c) Power share of the turbine relative to the compressor shaft power, (d) to (f) Relative humidity at the turbine outlet, (g) to (i) Pressure ratio of the turbine.

reduction of 8.1 %. As shown in Fig. 7 (d), topology T4 has a lower stack mass, lower humidifier mass and an increased compressor mass compared to the baseline (T1). The reason for this is the higher maximum pressure ratio of the compressor, which enables higher stack operating pressures and a more efficient humidification in the humidifier. A serial two-stage compressor is more beneficial for this aircraft than for the regional aircraft, because this aircraft operates at higher altitudes (see Fig. 6). The topologies T5 and T6 with a parallel two-stage compressor also achieve a mass reduction compared to the baseline, but lead to a higher mass than topology T4. The results for the volume are included in the supplementary information. Topologies T2 to T6 are found to reduce the overall volume by 4.8–15.5 % compared to the baseline, the most significant volume reduction is achieved with topology T4.

The efficiency of the investigated topologies is shown in Fig. 7 (e) and Fig. 7 (f). Compared to the baseline topology (T1), an added turbine (T2) increases the system efficiency by 5.9 percentage points during cruise. Topologies T4, T5 and T6 achieve even higher efficiencies during cruise and furthermore improve the efficiency during takeoff. The best efficiencies are achieved with topology T6 (parallel two-stage compressor with turbine), which combines the benefits of topology T2 (power recovery in turbine) and T5 (wide range of feasible compressor mass flows). This topology improves the cruise efficiency by 10.9 percentage points compared to the baseline. The drag throughout the flight mission is shown in the supplementary information. Topologies T2, T4, T5 and T6 result in a similar or somewhat lower drag as the baseline, while topology T3 has a slightly higher drag.

For the narrow-body aircraft, topologies T4 and T6 are selected for an in-depth analysis. Topology T4 performs best in terms of mass while Topology T6 achieves the highest efficiencies throughout the flight mission. The detailed results for these two topologies are shown in Fig. 10, the results for the remaining topologies are provided in the supplementary information. The efficiency curves of topologies T4 and T6 show the same trends, but topology T6 results in higher absolute values. The main reason for the lower efficiency of topology T4 is that it requires a higher compressor power (see Fig. 10 (e) and Fig. 10 (f)). This is the case because the serial compressor stages in T4 are designed based on a compressor map with a lower maximum efficiency (see Section 3.2.1). Moreover, topology T4 needs to use the surge bypass during takeoff, climb and cruise (see Fig. 10 (i)). Note that both stages of the serial two-stage compressor operate at the same actual mass flow $\dot{m}_{cp}$. The corrected mass flow $\dot{m}_{cp,red}$ of the second stage is different because of the different inlet conditions (see Eq. (14)). A smaller first stage could operate more efficiently during these flight phases, but would not be able to meet the mass flow and pressure ratio requirements of the descent phase. On the other hand, the two-stage parallel compressor in topology T6 is able to provide the required mass flow without using the surge bypass. This is achieved by having two stages with different sizes, and only using the larger stage 2 during descent (see Fig. 10 (k) and Fig. 10 (l)).

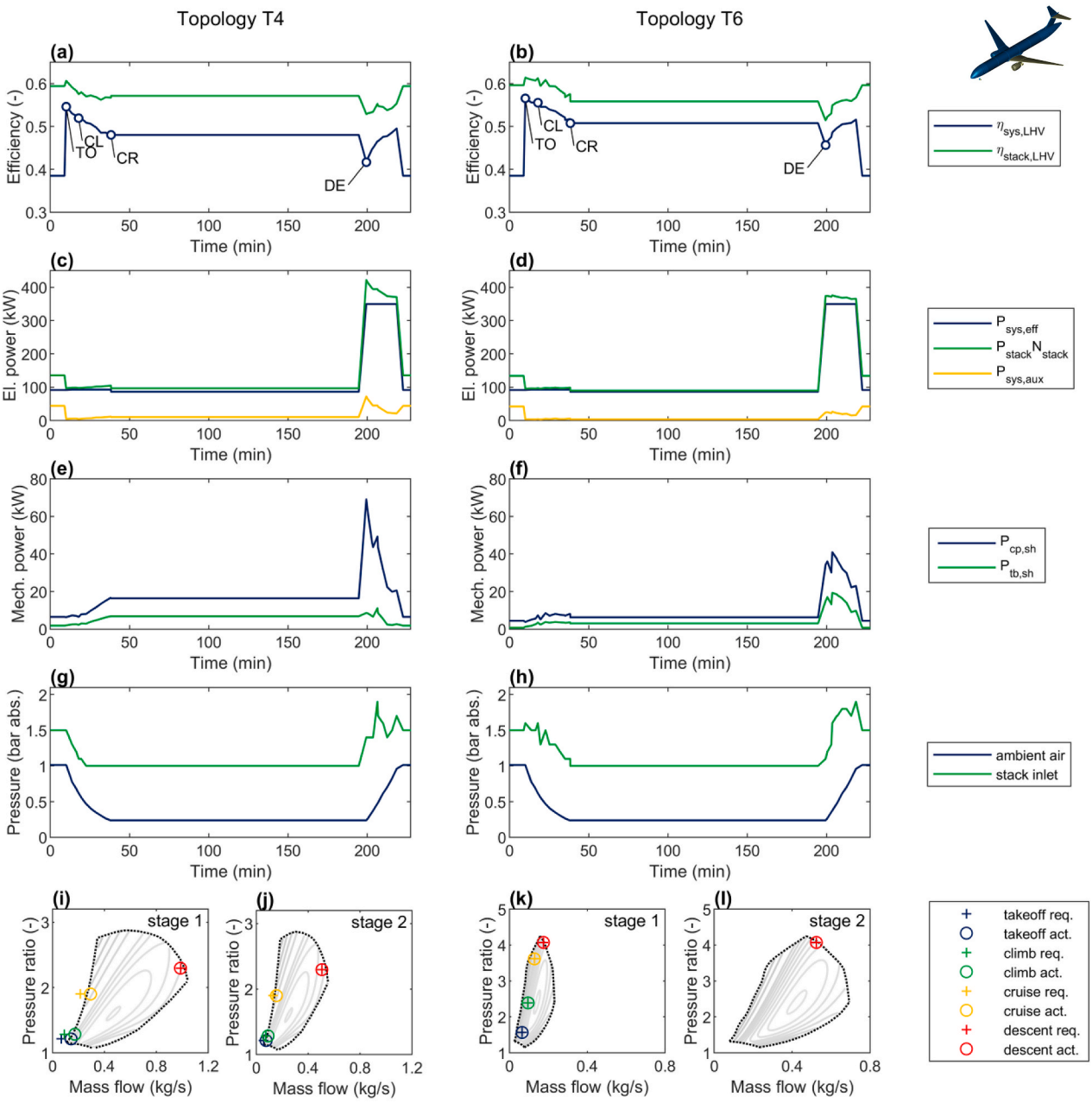

Fig. 10. Air supply system topologies for auxiliary power supply in narrow-body aircraft: detailed results for topology T4 (left) and T6 (right). The figure shows results for one of the aircraft's four identical fuel cell systems. (a) and (b): system efficiency $\eta_{sys,LHV}$ and stack efficiency $\eta_{stack,LHV}$, (c) and (d): electrical power, (e) and (f): mechanical shaft power, (g) and (h): pressures, (i) to (l): compressor maps (req.: required mass flow by stack, act: actual compressed mass flow for surge control). Aircraft image reproduced from Ref. [25].

The result of the stack pressure optimization is shown in Fig. 10 (g) and Fig. 10 (h). The main benefit of a serial two-stage compressor is that it can achieve higher overall pressure ratios. This benefit is used at the start of the descent phase, where the two serial stages provide an overall pressure ratio of $\Pi_{cp,s1} \cdot \Pi_{cp,s2} = 5.3$. During takeoff, climb and cruise, higher pressure ratios would not be beneficial as this would lead to an increased surge bypass mass flow (see Fig. 10 (i) and Fig. 10 (j)). The pressure ratio of the two parallel stages is limited to $\Pi_{cp,s1} = \Pi_{cp,s2} = 4.1$. This leads to a slightly better stack efficiency of topology T4 at the start of the descent phase at t = 199.4 min (see Fig. 10 (a) and Fig. 10 (b)). However, the overall efficiency of topology T4 is still lower than that of topology T6 even during descent because of the higher compressor power consumption.

Ultimately, the choice of the best topology depends on the design targets at the overall aircraft level. A serial two-stage compressor with a turbine (topology T4) is the best option if the goal is to minimize the overall mass (fuel cell system and tank). If the priority is to improve the system efficiency to minimize the fuel consumption, then a parallel two-stage compressor with turbines (topology T6) would be the most favorable option.

The sensitivity of the turbine power share to different compressor and turbine efficiency assumptions is shown in Fig. S10 of the supplementary information (analogously to Fig. 9). For this aircraft, the behavior is similar to that of the regional aircraft case, except there is no reduction in turbine power share if higher turbine efficiencies would be assumed. The reason for this is the higher flight altitude, which leads to higher compressor pressure ratios, increased compressor outlet temperatures and a more efficient heat transfer in the preheater. This leads

to higher turbine inlet temperatures and thus lower relative humidities at the turbine outlet.

5. Conclusions

This work investigated several advanced topologies for the air supply of fuel cells in aircraft applications. The investigated topologies use different compressor designs (single-stage, two serial stages, two parallel stages) and an optional turbine stage for exhaust expansion. The topologies were analyzed with a detailed thermodynamic model, which includes both direct effects related to the air supply system and indirect effects that arise from the coupling to the stacks, humidifier and thermal management system. The key findings can be summarized as follows:

1. To expand the fuel cell exhaust in a turbine stage without the risk of water condensation, the air needs to be heated in an additional heat exchanger ("preheater"). Nonetheless, the energy recovery benefits of a turbine stage are found to outweigh the mass of this additional heat exchanger by far.
2. The choice of the optimal air supply system topology depends on the aircraft type, specifically the maximum flight altitude and the difference between the minimum and maximum power that is required during the flight mission.
3. For the propulsion of regional aircraft, a single-stage compressor that is coupled to a turbine stage is the most favorable option. This topology can decrease the overall mass (fuel cell system and LH2 tank) by 4.5 % despite the added mass of the turbine and preheater.
4. At higher flight altitudes, two-stage compressor designs in combination with a turbine stage can provide additional benefits. For the investigated narrow-body aircraft, a serial two-stage compressor can decrease the mass of the fuel cell system and LH2 tank by 8.1 % (compared to a conventional single-stage layout). If the goal is to minimize the fuel consumption, then two parallel compressor stages are beneficial as they can efficiently compress a wide range of air flows. For the investigated aircraft, a parallel two-stage compressor can improve the efficiency during the cruise phase by 10.9 percentage points.

In summary, the results show that conventional single-stage compressors are not always optimal for fuel cells in aircraft applications. To this end, the integration of two-stage compressors and turbine stages is recommended as this can enable considerable improvements in specific power and efficiency. Radial two-stage compressors and turbine stages from the automotive industry can be a good starting point for this, but would require design modifications to meet the stringent requirements in aviation.

Several limitations in the developed approach remain to be addressed in future work. First, the developed model is steady-state. Transient simulations can be a useful extension to verify that the investigated air supply system topologies can meet the requirements for dynamic load changes. Second, the developed turbine model is based on several simplifications, specifically the assumption of a constant efficiency and the use of an averaged turbine map without explicit consideration of rotational speed limitations. Third, this work focusses on fixed-geometry turbines. Variable-geometry turbines are more complex, but could further improve the performance benefits of topologies with an added turbine stage.

CRediT authorship contribution statement

Matthias Schröder: Writing – original draft, Software, Methodology, Investigation, Formal analysis, Conceptualization. **Christoph Gentner:** Writing – review & editing, Supervision. **Syed-Asif Ansar:** Writing – review & editing, Supervision.

Declaration of competing interest

The authors declare that they have no known competing financial interests or personal relationships that could have appeared to influence the work reported in this paper.

Acknowledgements

This work was supported by the Federal Ministry for Digital and Transport of Germany via Projektträger Jülich and NOW GmbH (research project number 03B10704). The authors thank Daniel Silberhorn and Georgi Atanasov for providing information on the two investigated aircraft concepts. Furthermore, the authors thank their colleagues Pascal Albrecht, Stefan Fischer and Florian Becker for valuable discussions.

Appendix A. Supplementary data

Supplementary data to this article can be found online at https://doi.org/10.1016/j.enconman.2025.120936.

Data availability

Data will be made available on request.

References

[1] Klöwer M, Allen MR, Lee DS, Proud SR, Gallagher L, Skowron A. Quantifying aviation's contribution to global warming. Environ Res Lett 2021;16(10):104027. https://doi.org/10.1088/1748-9326/ac286e.
[2] International Renewable Energy Agency. *Decarbonising hard-to-abate sectors with renewables: Perspectives for the G7*. 2024. https://www.irena.org/-/media/Files/IRENA/Agency/Publication/2024/Apr/IRENA_G7_Decarbonising_hard_to_abate_sectors_2024.pdf (accessed April 23, 2025).
[3] Gössling S, Humpe A, Fichert F, Creutzig F. COVID-19 and pathways to low-carbon air transport until 2050. Environ Res Lett 2021;16(3):034063. https://doi.org/10.1088/1748-9326/abe90b.
[4] Adler EJ, Martins JRRA. Hydrogen-powered aircraft: fundamental concepts, key technologies, and environmental impacts. Prog Aerosp Sci 2023;141:100922. https://doi.org/10.1016/j.paerosci.2023.100922.
[5] Bergero C, Gosnell G, Gielen D, Kang S, Bazilian M, Davis SJ. Pathways to net-zero emissions from aviation. Nat Sustainability 2023;6(4):404–14. https://doi.org/10.1038/s41893-022-01046-9.
[6] Tiwari S, Pekris MJ, Doherty JJ. A review of liquid hydrogen aircraft and propulsion technologies. Int J Hydrogen Energy 2024;57:1174–96. https://doi.org/10.1016/j.ijhydene.2023.12.263.
[7] Hoelzen J, Silberhorn D, Schenke F, Stabenow E, Zill T, Bensmann A, et al. H2-powered aviation – optimized aircraft and green LH2 supply in air transport networks. Appl Energy 2025;380:124999. https://doi.org/10.1016/j.apenergy.2024.124999.
[8] Massaro MC, Pramotton S, Marocco P, Monteverde AHA, Santarelli M. Optimal design of a hydrogen-powered fuel cell system for aircraft applications. Energ Conver Manage 2024;306:118266. https://doi.org/10.1016/j.enconman.2024.118266.
[9] Airbus SE. *Press release: Airbus and MTU Aero Engines advance on hydrogen fuel cell technology for aviation*. 2025. https://www.airbus.com/en/newsroom/press-releases/2025-06-airbus-and-mtu-aero-engines-advance-on-hydrogen-fuel-cell-technology (accessed July 3, 2025).
[10] Airbus SE. *Press release: Airbus to trial in-flight auxiliary power entirely generated by hydrogen*. 2023. https://www.airbus.com/en/newsroom/press-releases/2023-06-airbus-to-trial-in-flight-auxiliary-power-entirely-generated-by (accessed July 14, 2023).
[11] Pratt JW, Klebanoff LE, Munoz-Ramos K, Akhil AA, Curgus DB, Schenkman BL. Proton exchange membrane fuel cells for electrical power generation on-board commercial airplanes. Appl Energy 2013;101:776–96. https://doi.org/10.1016/j.apenergy.2012.08.003.
[12] Schröder M, Becker F, Gentner C. Optimal design of proton exchange membrane fuel cell systems for regional aircraft. Energ Conver Manage 2024;308:118338. https://doi.org/10.1016/j.enconman.2024.118338.
[13] Zhang Y, Hu Z, Xu L, Liu H, Ye K, Li J, et al. Fuel cell system for aviation applications: modeling, parameter sensitivity, and control. Energ Conver Manage 2024;312:118555. https://doi.org/10.1016/j.enconman.2024.118555.
[14] Clean hydrogen joint undertaking. Strategic research and innovation agenda 2021-2027 - Annex 4. 2022. https://www.clean-hydrogen.europa.eu/about-us/key-documents/strategic-research-and-innovation-agenda_en (accessed Feb 12, 2024).
[15] Powercell Sweden AB. P System 100. https://powercellgroup.com/segments/aviation/ (accessed Feb 23, 2024).

[16] Kösters TL, Liu X, Kožulović D, Wang S, Friedrichs J, Gao X. Comparison of phase-change-heat-pump cooling and liquid cooling for PEM fuel cells for MW-level aviation propulsion. Int J Hydrogen Energy 2022;47(68):29399–412. https://doi.org/10.1016/j.ijhydene.2022.06.235.
[17] Huang X, Li Y, Ma H, Huang P, Zheng J, Song K. Fuel cells for multirotor unmanned aerial vehicles: a comparative study of energy storage and performance analysis. J Power Sources 2024;613:234860. https://doi.org/10.1016/j.jpowsour.2024.234860.
[18] Yin C, Hua S, Nie W, Yang H, Tang H. Comparative study on air-cooled fuel cell stacks with metal and graphite bipolar plate designs for unmanned aerial vehicles. eTransportation 2024;21:100344. https://doi.org/10.1016/j.etran.2024.100344.
[19] Massaro MC, Biga R, Kolisnichenko A, Marocco P, Monteverde AHA, Santarelli M. Potential and technical challenges of on-board hydrogen storage technologies coupled with fuel cell systems for aircraft electrification. J Power Sources 2023;555:232397. https://doi.org/10.1016/j.jpowsour.2022.232397.
[20] Sparano M, Sorrentino M, Troiano G, Cerino G, Piscopo G, Basaglia M, et al. The future technological potential of hydrogen fuel cell systems for aviation and preliminary co-design of a hybrid regional aircraft powertrain through a mathematical tool. Energ Conver Manage 2023;281:116822. https://doi.org/10.1016/j.enconman.2023.116822.
[21] Sain CK, Hänsel J, Kazula S. Conceptual design of air and thermal management in a nacelle-integrated fuel cell system for an electric regional aircraft. In: Presented at AIAA AVIATION 2023 Forum; 2023. https://doi.org/10.2514/6.2023-3875.
[22] Moslehi A, Kandidayeni M, Hébert M, Kelouwani S. Investigating the impact of a fuel cell system air supply control on the performance of an energy management strategy. Energ Conver Manage 2025;325:119374. https://doi.org/10.1016/j.enconman.2024.119374.
[23] Campanari S, Manzolini G, Beretti A, Wollrab U. Performance assessment of turbocharged pem fuel cell systems for civil aircraft onboard power production. J Eng Gas Turbines Power, 130(2), 2008, doi: 10.1115/1.2772636.
[24] Atanasov G. "Comparison of Sustainable Regional Aircraft Concepts," presented at Deutscher Luft- und Raumfahrtkongress (conference). Germany: Dresden; 2022.
[25] Ramm J, Rahn A, Silberhorn D, Wicke K, Wende G, Papantoni V, et al. Assessing the feasibility of hydrogen-powered aircraft: a comparative economic and environmental analysis. J Aircr 2024;61(5):1337–53. https://doi.org/10.2514/1.C037463.
[26] Avions de Transport Régional GIE. ATR72-600. https://www.atr-aircraft.com/our-aircraft/atr-72-600/ (accessed Nov 28, 2023).
[27] Gohardani AS, Doulgeris G, Singh R. Challenges of future aircraft propulsion: a review of distributed propulsion technology and its potential application for the all electric commercial aircraft. Prog Aerosp Sci 2011;47(5):369–91. https://doi.org/10.1016/j.paerosci.2010.09.001.
[28] Bender D. Integration of exergy analysis into model-based design and evaluation of aircraft environmental control systems. Energy 2017;137:739–51. https://doi.org/10.1016/j.energy.2017.05.182.
[29] Vietze M, Weiland S. System analysis and requirements derivation of a hydrogen-electric aircraft powertrain. Int J Hydrogen Energy 2022;47(91):38793–810. https://doi.org/10.1016/j.ijhydene.2022.09.052.
[30] Fischer Fuel Cell Compressor AG. Fuel Cell Compressor Brochure. 2025. https://www.fischer-fuelcell-compressor.com/fileadmin/user_upload/02_FFCC/DOKUMENTE/20250305_3_FFCC_Teaser_Brochure_EN.pdf (accessed Oct 9, 2025).
[31] Garrett Motion Inc. Performance Catalogue Vol. 9. https://www.garrettmotion.com/wp-content/uploads/2024/01/Garrett_Performance_Catalog_01082024.pdf (accessed September 27, 2024).
[32] Mao H, Tang X, Liu J, Xu S. Numerical and experimental investigation on condensation inside a turbine designed for an 100 kW polymer electrolyte membrane fuel cell system. Int J Hydrogen Energy 2024;50:945–60. https://doi.org/10.1016/j.ijhydene.2023.09.237.
[33] Wittmann T, Lück S, Bode C, Friedrichs J. Modelling the condensation phenomena within the radial turbine of a fuel cell turbocharger. Int J Turbomachinery, Propulsion and Power, 6(3), doi: 10.3390/ijtpp6030023.
[34] Yanbin L, Weilin Z, Yangjun Z, Shuyong Z, Junyue Z, Xuemin H. A matching method for two-stage turbocharging system. J Eng Gas Turbines and Power, 137 (2), 2014, doi: 10.1115/1.4028387.
[35] Palmer DL, Waterman WF. Design and development of an advanced two-stage centrifugal compressor. J Turbomach 1995;117(2):205–12. https://doi.org/10.1115/1.2835648.
[36] Schröder M, Becker F, Kallo J, Gentner C. Optimal operating conditions of PEM fuel cells in commercial aircraft. Int J Hydrogen Energy 2021;46(66):33218–40. https://doi.org/10.1016/j.ijhydene.2021.07.099.
[37] Struchtrup H. Thermodynamics and energy conversion. 1st ed. Berlin Heidelberg: Springer-Verlag; 2014.
[38] Rotrex A/S. Rotrex C-range C38 supercharger. https://www.rotrexshop.com/wp-content/uploads/2021/12/Rotrex_Technical_Datasheet_C38_Rev6.0.pdf (accessed Feb 21, 2024).
[39] Mecrow BC, Jack AG. Efficiency trends in electric machines and drives. Energy Policy 2008;36(12):4336–41. https://doi.org/10.1016/j.enpol.2008.09.042.
[40] Jensen J-P, Kristensen AF, Sorenson SC, Houbak N. "Mean Value modeling of a small turbocharged diesel engine," 1991. DOI: 10.4271/910070.
[41] Moraal P, Kolmanovsky I. Turbocharger modeling for automotive control applications. SAE Technical Paper 1999. https://doi.org/10.4271/1999-01-0908.
[42] Botros KK, Henderson JF. Developments in centrifugal compressor surge control: a technology assessment. In: presented at ASME 1993 International Gas Turbine and Aeroengine Congress and Exposition; 1993. https://doi.org/10.1115/93-GT-008.
[43] Dakshina Murty V. Turbomachinery: concepts, applications, and design. Milton, United Kingdom: Taylor & Francis Group; 2018.
[44] Schröter J, Frank D, Radke V, Bauer C, Kallo J, Willich C. Influence of low inlet pressure and temperature on the compressor map limits of electrical turbo chargers for airborne fuel cell applications. Energies, 15(8), doi: 10.3390/en15082896.
[45] Rotrex A/S. Rotrex EK40 Fuel Cell Compressor. https://rotrex-fuel-cell-compressor.com/wp-content/uploads/2022/05/Rotrex-Technical-Datasheet-EK40-Rev1.2.pdf (accessed Jul 28, 2022).
[46] Feneley AJ, Pesiridis A, Andwari AM. Variable geometry turbocharger technologies for exhaust energy recovery and boosting-a review. Renew Sustain Energy Rev 2017;71:959–75. https://doi.org/10.1016/j.rser.2016.12.125.
[47] Bozza F, De Bellis V. Steady modeling of a turbocharger turbine for automotive engines. J Eng Gas Turbines Power, 136(1), 2013, doi: 10.1115/1.4025263.
[48] European Union Aviation Safety Agency (EASA). "CS-25 certification specifications and acceptable means of compliance for large aeroplanes. Amendment 24, section CS-25.1043," 2020.
[49] Torenbeek E. "Appendix B: International Standard Atmosphere," in Advanced Aircraft Design. Chichester, United Kingdom: John Wiley and Sons, Ltd.; 2013. p. 397–8.
[50] Epstein AH. Aeropropulsion for commercial aviation in the twenty-first century and research directions needed. AIAA J 2014;52(5):901–11. https://doi.org/10.2514/1.J052713.